

THE HELLAS2XMM SURVEY. VII. THE HARD X-RAY LUMINOSITY FUNCTION OF AGN UP TO $Z=4$: MORE ABSORBED AGN AT LOW LUMINOSITIES AND HIGH REDSHIFTS

F. LA FRANCA¹, F. FIORE², A. COMASTRI³, G.C. PEROLA¹, N. SACCHI¹, M. BRUSA⁴, F. COCCIA², C. FERUGLIO², G. MATT¹, C. VIGNALI⁵, N. CARANGELO⁶, P. CILIEGI³, A. LAMASTRA¹, R. MAIOLINO⁷, M. MIGNOLI³, S. MOLENDI⁸, S. PUCETTI²

Received 2005 May 26; accepted 2005 August 15

ABSTRACT

We have determined the cosmological evolution of the density of active galactic nuclei (AGN) and of their N_{H} distribution as a function of the un-absorbed 2–10 keV luminosity up to redshift 4. We used the HELLAS2XMM sample combined with other published catalogs, yielding a total of 508 AGN. Our best fit is obtained with a luminosity-dependent density evolution (LDDE) model where low luminosity ($L_{\text{X}} \sim 10^{43}$ erg s⁻¹) AGN peak at $z \sim 0.7$, while high luminosity AGN ($L_{\text{X}} > 10^{45}$ erg s⁻¹) peak at $z \sim 2.0$. A pure luminosity evolution model (PLE) can instead be rejected.

There is evidence that the fraction of absorbed ($N_{\text{H}} > 10^{22}$ cm⁻²) AGN decreases with the intrinsic X-ray luminosity, and increases with the redshift.

Our best fit solution provides a good fit to the observed counts, the cosmic X-ray background, and to the observed fraction of absorbed AGN as a function of the flux in the $10^{-15} < S_{2-10} < 10^{-10}$ erg cm⁻² s⁻¹ range. We find that the absorbed, high luminosity ($L_{\text{X}} > 10^{44}$ erg s⁻¹) AGN have a density of 267 deg⁻² at fluxes $S_{2-10} > 10^{-15}$ erg cm⁻² s⁻¹. Using these results, we estimate a density of supermassive black holes in the local Universe of $\rho_{\text{BH}} = 3.2 h_{70}^2 \times 10^5 \text{ M}_{\odot} \text{ Mpc}^{-3}$, which is consistent with the recent measurements of the black hole mass function in the local galaxies.

Subject headings: diffuse radiation — galaxies: active — galaxies: evolution — quasars: general — surveys — X-rays: diffuse background

1. INTRODUCTION

The understanding of the history of accretion in the Universe and of the formation of massive black holes and their host galaxies relies on the measurement of the active galactic nuclei (AGN) space density and evolution.

According to the AGN unified model (Antonucci 1993) the viewing angle between the observer and the symmetry axis of the nuclear structure is responsible for the different classification. In type 1 AGN the central engine is directly visible. Both the broad and narrow line emitting regions are detected in the optical spectra along with a soft un-absorbed X-ray spectrum. On the contrary, a type 2 AGN classification arises when the broad line region and the soft X-rays are obscured by a dusty torus.

Until a few years ago the best measurements of the cosmological evolution of the AGN luminosity function were essentially limited to optically (e.g. La Franca & Cristiani 1997, Croom et al. 2004), and soft X-rays (e.g. Maccacaro et al. 1991, Miyaji et al. 2000) selected type 1 AGN. While there is evidence that type 2 AGN are

about a factor four more numerous than type 1 AGN (e.g. Maiolino & Rieke 1995; Risaliti et al. 1999), their relative space density beyond the local Universe is basically unknown. Assuming that the cosmological evolution of type 1 and 2 AGN is the same, it was possible to simultaneously reproduce the X-ray background spectrum and the X-ray counts (e.g. Setti & Woltjer 1989; Comastri et al. 1995). This simple picture was later slightly modified in models where the fraction of type 2 AGN was assumed to increase towards higher redshifts (e.g. Pompilio et al. 2000, Gilli et al. 1999, 2001). The selection of complete samples of type 2 AGN is a difficult task. In the optical they are often so dim that only the light of the host galaxy is visible; at $z > 1$ even the latter has usually $R > 24$. In the soft X-rays bands even hydrogen column densities, N_{H} , of the order of 10^{21-22} cm⁻² may strongly suppress the flux. In the hard (2–10 keV) X-rays type 2 AGN selection is less biased against, though the absorption due to large N_{H} column densities (10^{23-24} cm⁻²) is not negligible especially at low redshifts.

Early attempts to compute the hard X-ray luminosity function, based on *ASCA* and *Beppo-SAX* observations (Boyle et al., 1998; La Franca et al. 2002 respectively) indicated a strong evolution for type 1 AGN, with a rate similar to that measured in the soft X-rays. Unfortunately the low spatial resolution of the X-ray detectors prevented an unambiguous identification of the type 2 AGN optical counterparts, thus hampering a reliable determination of the type 2 AGN space density.

Thanks to the high sensitivity and spatial resolution of the hard X-ray detectors on board *XMM-Newton* and *Chandra*, it has become possible to carry out AGN surveys less biased against X-ray absorption and with more secure optical identifications.

¹ Dipartimento di Fisica, Università degli Studi "Roma Tre", Via della Vasca Navale 84, I-00146 Roma, Italy.

² INAF, Osservatorio Astronomico di Roma, Via , I-00100 Monteporzio, Italy

³ INAF, Osservatorio Astronomico di Bologna, Via Ranzani 1, I-40127 Bologna, Italy

⁴ Max Planck Institut für Extraterrestrische Physik (MPE), Giessenbachstrasse, Postfach 1312, 85741 Garching, Germany

⁵ Dipartimento di Astronomia, Università di Bologna, Via Ranzani 1, I-40127 Bologna, Italy

⁶ Università di Milano-Bicocca, Piazza della Scienza 3, I-20126 Milano, Italy

⁷ INAF, Osservatorio Astrofisico di Arcetri, Largo Fermi 5, I-50125 Firenze, Italy

⁸ INAF, IASF, Via Bassini 15, I-20133, Milano, Italy

However, already at fluxes fainter than $S_{2-10} \sim 10^{-14}$ erg cm $^{-2}$ s $^{-1}$, a sizeable fraction of the X-ray sources have optical magnitudes fainter than the spectroscopic limit of 8–10 meter class optical telescopes, and thus the measure of their distance has to rely on photometric redshifts, when it is not impossible altogether.

For these reasons, although the *Chandra* Deep Field North (CDF-N; Alexander et al. 2003) and the *Chandra* Deep Field South (CDF-S; Giacconi et al. 2002) surveys have resolved a fraction of the 2–10 keV XRB as large as 85–90% (see also Brandt and Hasinger 2005), a clear picture of the AGN evolution able to reproduce the whole set of observational constraints (i.e. soft and hard X-ray counts, X-ray background, N_H and redshift distributions) is still missing.

Attempts to take into account the redshift incompleteness of X-ray selected AGN have been carried out by Cowie et al. (2003), Fiore et al. (2003), Barger et al. (2005) combining data from deep and shallow surveys. They independently demonstrated that the AGN number density for luminosities lower than $\sim 10^{44}$ erg s $^{-1}$ peaks at a lower redshift than that of high luminosity objects. Making use of an almost complete sample of 247 AGN from *Chandra*, *ASCA* and *HEAO1* surveys above a limiting flux of $S_{2-10} > 3.8 \times 10^{-15}$ erg cm $^{-2}$ s $^{-1}$ Ueda et al. (2003) were able to estimate the hard X-ray luminosity function (HXLf) up to $z = 3$. They found that the fraction of the X-ray absorbed AGNs decreases with the intrinsic luminosity and that the evolution of the AGN HXLf is best described by a luminosity-dependent density evolution (LDDE). Very similar results were also obtained by Hasinger et al. (2005) using an almost complete sample of soft X-ray selected type 1 AGN.

In this paper we expand the study carried out by Fiore et al. (2003) with the aim to compute the shape and evolution of the HXLf and N_H distribution of all AGN with $N_H < 10^{25}$ cm $^{-2}$ up to $z \sim 4$. To reach such a goal it is necessary to cover the widest possible range in the L_X - z - N_H space, and to take into account all possible selection effects. For these reasons we have used a large AGN sample (about 500 objects) four times deeper than the Ueda et al. (2003) sample. A new method to correct for the spectroscopic incompleteness of faint X-ray sources is presented and discussed in detail. The selection effects due to X-ray absorption are also specifically discussed and estimated by an appropriate X-ray “K-correction” term.

The paper is structured as follows: in Section 2 we describe the adopted X-ray samples; in Section 3 the method to compute the HXLf is discussed. The results are presented in Section 4, discussed in Section 5 and summarized in the last section.

Throughout this paper we call AGN all objects with an intrinsic (corrected for N_H absorption) 2–10 keV X-ray luminosity larger than 10^{42} erg s $^{-1}$. In the last few years evidence for a mismatch between optical (Type 1/2) and X-ray (un-absorbed/absorbed) classification has emerged (e.g. Fiore et al. 2000). In this paper we refer to AGN1 if broad emission lines (rest frame FWHM > 2000 km s $^{-1}$) are present, while all remaining objects (with or without narrow emission lines in the optical spectrum) are called AGN2. If the rest frame column density is larger than 10^{22} cm $^{-2}$ the AGN is classified as *absorbed*. The adopted limit is well above

TABLE 1
THE SAMPLES

Sample (1)	Flux limit (2)	N_S (3)	N_{sp} (4)	R_{lim} (5)
HEAO1	2.9×10^{-11}	31	31	...
AMSSn	3.0×10^{-13}	74	74	...
HBS28	2.2×10^{-13}	27	27	...
H2XMM ^a	8.0×10^{-15}	120	103 (93)	23.65
H2XMM ^b	8.0×10^{-15}	110	44	21.40
Lockman	2.6×10^{-15}	55	41 (39)	23.50
CDFN	1.0×10^{-15}	146	108 (102)	24.65
CDFS	1.0×10^{-15}	127	102 (98)	25.00

NOTE. — In column (2) we give the flux limit of the samples in units erg cm $^{-2}$ s $^{-1}$. In column (3) we give the total number of sources. In column (4) we give the number of sources brighter than the spectroscopic limit (in parenthesis those having redshift). In column (5) we give the spectroscopic completeness magnitude.

^a1df sample (Fiore et al. 2003).

^b0.5df sample (Cocchia et al. 2005).

the typical X-ray absorption by host galaxy gas (disk, starburst regions, etc.) thus ensuring that the measured column is most likely related to nuclear obscuration. Unless otherwise stated, all quoted errors are at the 68% confidence level. We assume $H_0 = 70$ km s $^{-1}$ Mpc $^{-1}$, $\Omega_m = 0.3$ and $\Omega_\Lambda = 0.7$.

2. SAMPLES

In order to cover the widest possible range of luminosities and redshifts we combined the HELAS2XMM sample (Fiore et al. 2003) with other existing flux limited samples which allowed the estimates of the rest frame N_H column density of each AGN. Whenever possible, the column density and the photon index (Γ) were determined with a proper spectral analysis. Otherwise, we assumed $\Gamma = 1.8$, and used the hardness ratio to measure the $z=0$ column density (N_{H0} , see also the discussion about the uncertainties of this approach in §4.1.1). The rest frame column density (N_H) was then estimated by the relation $\text{Log}(N_H) = \text{Log}(N_{H0}) + 2.42 \text{Log}(1+z)$, which makes use of the Morrison & McCammon (1983) cross sections, including also the effects of the absorption edges, and assumes solar abundances from Anders & Grevesse (1989).

For those samples whose optical spectroscopic identifications are incomplete, we chose the optical magnitude limit at which the samples are almost spectroscopically complete. The incompleteness is 6% in the HELAS2XMM, Lockman, CDF-N and CDF-S samples). In these cases (as the X-ray-optical flux distribution of the sources without redshift is almost similar to that of the spectroscopically identified sources, and the fraction of the unidentified sources is small) the sky coverage has been reduced according to the fraction of spectra available. Table 1 contains a summary of the characteristics of each sample. The distribution in the L_X - z space of all AGN from the spectroscopically complete sub-samples used in our analysis are shown in Figure 1, while Figure 2 shows their distribution in the S_X -R plane.

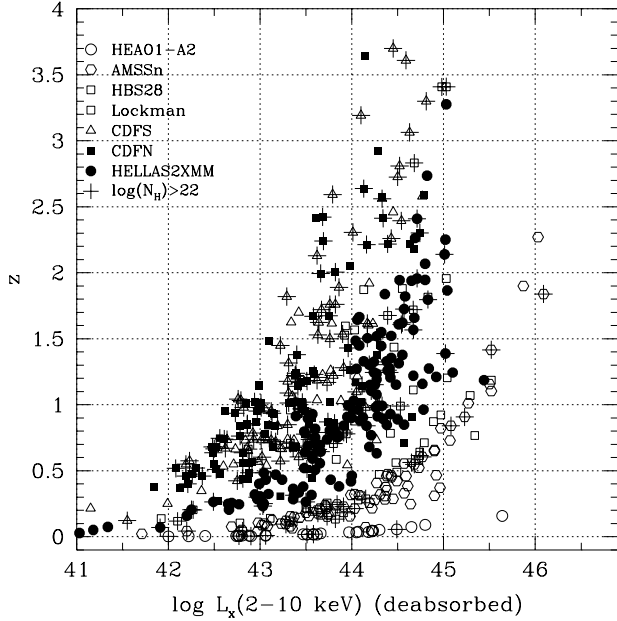


FIG. 1.— L_X - z plane for all AGN used in this analysis. Different symbols corresponds to different surveys, as labeled in the top left corner. Absorbed sources are also highlighted by a cross.

2.1. The HELLAS2XMM sample

We used the HELLAS2XMM 1df (1 degree field) sample (Fiore et al. 2003) plus the recently available extension of 0.5 deg² (HELLAS2XMM 0.5df Cocchia et al. 2005). The HELLAS2XMM 1df sample contains 122 sources, serendipitously detected in five XMM-Newton fields with $S_X(2-10 \text{ keV}) > 0.8 \times 10^{-14} \text{ erg cm}^{-2} \text{ s}^{-1}$. In our analysis we used the fluxes and the column densities measured by X-ray spectral analysis (Perola et al. 2004). Among the 122 sources we discarded one star (object n. 0537006) and one extended source (object n. 26900013). For three sources with low signal-to-noise the hardness ratio and redshift were used to estimate the rest frame N_H . In summary, the sample contains 120 sources, 115 optically identified, and 95 with measured redshift and optically classified. We restricted our analysis to the sources brighter than $R=23.65$. Down to this limit 93 out of 103 sources have been spectroscopically identified.

The HELLAS2XMM 0.5df sample consists of 110 objects brighter than $S_X(2-10 \text{ keV}) = 8 \times 10^{-15} \text{ erg cm}^{-2} \text{ s}^{-1}$. Among them, 44 sources brighter than $R=21.4$ (but otherwise randomly selected) have been spectroscopically identified.

2.2. The Piccinotti sample

The Piccinotti sample is the brightest included in our analysis. It has been obtained through observations carried out by the HEAO1 satellite, and contains 31 sources selected over an area of 26919 deg² down to $S_X(2-10 \text{ keV}) = 2.9 \times 10^{-11} \text{ erg cm}^{-2} \text{ s}^{-1}$ (Piccinotti et al. 1982). The column densities have been taken from the literature, and are derived from X-ray spectral analyses.

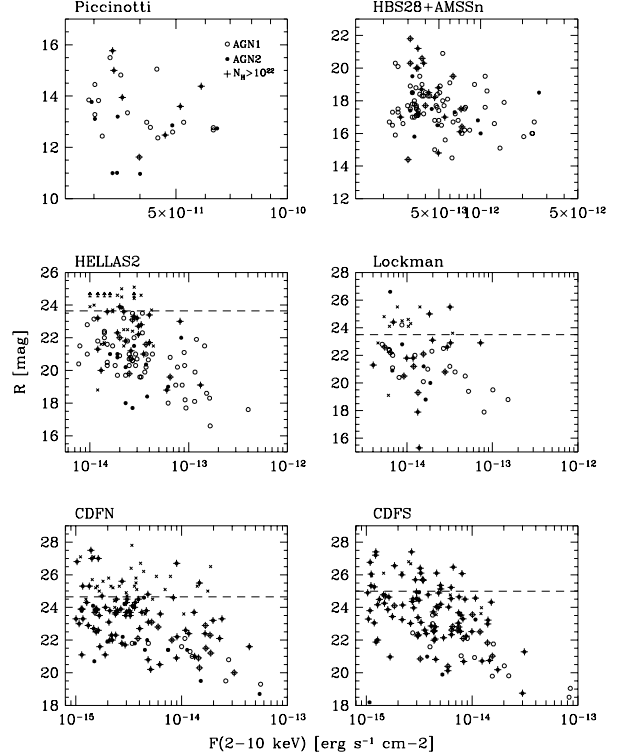


FIG. 2.— R-band magnitude versus the 2–10 keV X-ray flux for all sources of the samples used in this analysis. The dashed lines are the spectroscopic limits of completeness adopted in our analysis.

2.3. The AMSSn sample

The AMSSn sample consists of 74 AGN at fluxes brighter than $S_X(2-10 \text{ keV}) = 3 \times 10^{-13} \text{ erg cm}^{-2} \text{ s}^{-1}$ (Akiyama et al. 2003). The total area covered is 45 deg² at the fainter fluxes and rises up to $\sim 69 \text{ deg}^2$ at bright fluxes. The N_H column densities have been derived from the hardness ratios values.

2.4. The HBS28 sample

The HBS28 sample (Caccianiga et al. 2004) consists of 27 AGN and 1 star selected in the 4.5–7.5 keV band. The sources are brighter than $S_X(2-10 \text{ keV}) = 2.2 \times 10^{-13} \text{ erg cm}^{-2} \text{ s}^{-1}$ (assuming $\Gamma=1.8$) and have been selected over 82 XMM-Newton pointed fields, corresponding to a total of 9.756 deg². All sources have been spectroscopically identified, and their column densities have been measured through X-ray spectral fits.

2.5. The Lockman Hole sample

The Lockman Hole sample consists of 55 sources selected within the 12 arcmin radius of the XMM-Newton observation. The sources are brighter than $S_X(2-10 \text{ keV}) = 2.6 \times 10^{-15} \text{ erg cm}^{-2} \text{ s}^{-1}$ (Baldi et al. 2002). Optical identifications and X-ray spectral fits are from Mainieri et al. (2002). Spectroscopic redshifts and classifications have been obtained for 41 objects, while 3 sources have photometric redshifts. We restricted our analysis to the sources brighter than $R=23.50$. Down to this limit 39 out of 41 sources have been spectroscopically

identified.

2.6. The CDF-N sample

In order to reach almost spectroscopic completeness we have selected an X-ray bright subsample in the CDF-N. The subsample consists of 146 sources (see Table 1) selected within the 10 arcmin radius of the *Chandra* observation (Alexander et al. 2003). The sky coverage reaches $S_X(2-10 \text{ keV}) > 10^{-15} \text{ erg cm}^{-2} \text{ s}^{-1}$ in the inner 5.85 arcmin radius, $S_X(2-10 \text{ keV}) > 2.49 \times 10^{-15} \text{ erg cm}^{-2} \text{ s}^{-1}$ in the annulus between 5.85 and 6.5 arcmin radii, and $S_X(2-10 \text{ keV}) > 3.61 \times 10^{-15} \text{ erg cm}^{-2} \text{ s}^{-1}$ in the annulus between 6.5 and 10.0 arcmin radii. We used both spectroscopic and spectro-photometric identifications and redshifts available from the literature (Barger et al. 2003). We restricted our analysis to sources brighter than $R=24.65$. Down to this limit 102 out of 108 sources have been spectroscopically identified. The N_H column densities have been derived from the hardness ratios.

2.7. The CDF-S sample

Although the CDF-S has been observed for 1 Ms instead of the 2 Ms spent in the CDF-N, we selected a spectroscopically complete X-ray bright subsample with the same sky coverage as for the CDF-N. Indeed, at our adopted flux limits, the difference in the exposure time does not affect the sky coverage. The sample consists of 127 sources (see Table 1; Giacconi et al. 2002 and Alexander et al. 2003). We used both spectroscopic and spectro-photometric redshifts available from the literature (Szokoly et al. 2004; Zheng et al. 2004). Moreover, given that both Szokoly et al. (2004) and Zheng et al. (2004) identifications are based on the X-ray source catalogue of Giacconi et al. (2002), we have revised some optical/X-ray associations according to the improved astrometry provided by Alexander et al. (2003). We restricted our analysis to sources brighter than $R=25.00$. Down to this limit 98 out of 102 sources have been spectroscopically identified. The N_H column densities have been derived from the hardness ratios.

3. METHOD

We searched for a functional fit to the density of the AGN as a function of the un-absorbed 2–10 keV luminosity (L_X), the rest frame absorbing column density (N_H), and the redshift (z). The method is based on the comparison, through χ^2 estimators, of the observed and expected numbers of AGN (in the L_X - z space) and of the N_H distributions, obtained from computations which take into account all the observational selection effects of the samples.

Once a HXLF evolution model is assumed, the number of expected AGNs (E) in a given bin of the L_X - z - N_H space is the result of the sum, over the number of samples N_{samp} , of the expected number of AGN in each sample taking into account the area coverage of each i th sample $\Omega_i(L, N_H, z)$, the N_H distribution $f(L_X, z; N_H)$, and a completeness function $g(L_X, z, N_H, R_i)$, where R_i is the spectroscopic limit of completeness of the i th sample:

$$E = \sum_{i=1}^{N_{\text{samp}}} \int \int \int \Phi(L_X, z) f(L_X, z; N_H) \times g(L_X, z, N_H, R_i) \Omega_i(L, N_H, z) \frac{dV}{dz} d\text{Log} L_X dz dN_H. \quad (1)$$

3.1. The shape of the Luminosity Function

In order to describe the evolution of the AGN, we used standard functional forms, such as the pure luminosity evolution (PLE) model and a luminosity-dependent density evolution (LDDE) model (see next Section and, e.g., Boyle et al. 1998; Miyaji et al. 2000; La Franca et al. 2002; Ueda et al. 2003). The HXLF, representing the number density per unit comoving volume and per unit $\text{Log } L_X$, as a function of L_X and z , was expressed as:

$$\frac{d\Phi(L_X, z)}{d\text{Log} L_X}. \quad (2)$$

We adopted a smoothly-connected two power-law form to describe the present-day HXLF,

$$\frac{d\Phi(L_X, z=0)}{d\text{Log} L_X} = A[(L_X/L_*)^{\gamma_1} + (L_X/L_*)^{\gamma_2}]^{-1}. \quad (3)$$

3.2. The K-correction

In order to convert the observed 2–10 keV fluxes (S_X) to the intrinsic 2–10 keV luminosities (L_X) and vice-versa, for each observed or “expected” AGN with a given N_H , a K-correction has been computed by assuming a photon index $\Gamma = 1.8$, an exponential cutoff (e^{-E/E_C}) at $E_C = 200 \text{ keV}$, and the corresponding photoelectric absorption (see §4.1.1 for a discussion on the use of different K-corrections).

3.3. The completeness function

All the faint samples used in our analysis (HEL-LAS2XMM, Lockmann, CDF-S, CDF-N) are nearly spectroscopically complete down to a certain optical limit magnitude ($R=21.4-25$, see Table 1). In order to compute the number of expected AGN in a certain bin of the L_X - z - N_H space, we introduced the *completeness function* $g(L_X, z, N_H, R)$ which provides the probability that a given AGN with luminosity L_X , redshift z and column density N_H , had an apparent R-band magnitude brighter than the spectroscopic limits of completeness R of each sample.

For this reason we derived an empirical relationship between the un-absorbed X-ray luminosity L_X and the optical luminosity L_R ⁹ for AGN1 and AGN2, and measured their spread (see Figure 3). For AGN1 we found:

$$\text{Log} L_R = 0.959(\pm 0.025) \times \text{Log} L_X + 2.2(\pm 1.1), \quad (4)$$

with a 1σ dispersion of 0.48 (in $\text{Log} L_R$ units) around the best fit solution. The linear correlation coefficient is

⁹ The L_R luminosity is in $\text{erg s}^{-1} (\nu L_\nu)$, computed at 660 nm, where the flux is $f[\text{erg s}^{-1} \text{ cm}^{-2} \text{ Hz}^{-1}] = 2.84 \times 10^{-20} \times 10^{-0.4R}$ (Zombeck 1990).

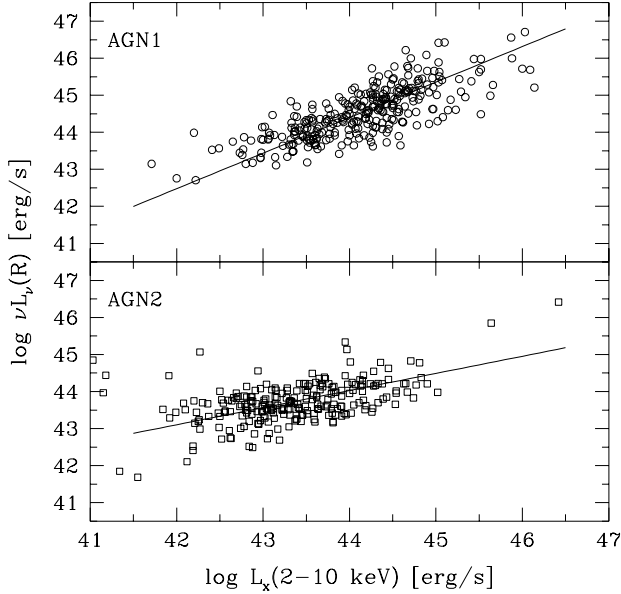


FIG. 3.— $\text{Log}L_X\text{--}\text{Log}L_R$ relation for optical AGN1 and AGN2. The continuous lines correspond to eq. 4 and 5.

$r=0.773$, corresponding to a negligible ($<10^{-13}$) probability that the data are consistent with the null hypothesis of zero correlation. For AGN2 a flatter relation was found:

$$\text{Log}L_R = 0.462(\pm 0.026) \times \text{Log}L_X + 23.7(\pm 1.1), \quad (5)$$

with a 1σ dispersion of 0.40 (in $\text{Log}L_R$ units), and a linear correlation coefficient $r=0.462$, again corresponding to a negligible ($<2 \times 10^{-13}$) probability that the data are consistent with the null hypothesis of zero correlation. In order to compute the above relationships a linear least squared method with errors (assumed 0.2 dex) in both axes has been used. The difference between the two relations should be attributed to the dominance in the optical of the AGN component in the AGN1, which produces an almost linear relationship between X-ray and optical luminosity (see La Franca et al., 1995 for similar results in the soft X-rays). In AGN2, where the nucleus is obscured, the optical luminosity is instead dominated by the host galaxy (see also Fiore et al. 2003).

For each pair of un-absorbed X-ray luminosity and redshift, the above relationships (*with their spreads*) can be used to compute the probability of an AGN to appear brighter than a certain optical magnitude, and thus be spectroscopically identified. The observed spreads of the two relationships are due to a combination of the intrinsic spread with the observational uncertainties. Given our aims, both effects should be taken into account, and we have thus not subtracted the contribution of the observational uncertainties from the spread estimates. To choose which $L_X\text{--}L_R$ relationship to use (eq. 4 or eq. 5), we need also to know the probability of an AGN to appear as an AGN1 (or, its complement, an AGN2) as a function of L_X , N_H and z : $Q1(L_X, z, N_H)$. This probability was estimated from the sample itself as described below.

Figure 4 shows the distribution of the observer frame column density N_{H0} as a function of L_X for AGN1 and

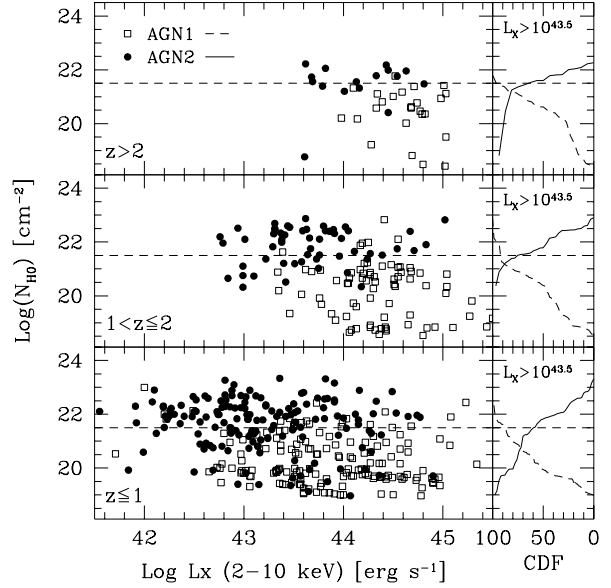


FIG. 4.— $\text{Log}L_X\text{--}\text{Log}N_{H0}$ plane at $z \leq 1$ (bottom), $1 < z \leq 2$ (middle), $z > 2$ (up). Open squares are optical AGN1, filled circles are optical AGN2. On the right side the dashed lines are the cumulative distribution functions of the N_{H0} values for AGN1 with $L_X > 10^{43.5} \text{ erg s}^{-1}$, while the continuous lines are the complement of the cumulative distribution function of the N_{H0} values for AGN2 with $L_X > 10^{43.5} \text{ erg s}^{-1}$.

AGN2, in three redshift intervals. Here we do not use the rest frame N_H , but instead the observer frame N_{H0} which is equivalent to an hardness ratio (see also Hasinger 2003). As can be seen in Figure 5, the probability to find an AGN1 is not only dependent on N_{H0} , but depends also on the luminosity. The probability to find an AGN1 increases with increasing luminosities, and there is a relevant fraction of low luminosity ($L_X < 10^{43} \text{ erg s}^{-1}$) un-absorbed objects which are AGN2, while a fraction of the high luminosity ($L_X > 10^{45} \text{ erg s}^{-1}$) absorbed objects are AGN1. This result, if it is not due to the contamination by the galaxy light in the lower luminosity AGN2, is against the simplest version of the AGN unified model. The analysis of this issue is beyond the scope of this paper (see Panessa & Bassani 2002, Page et al. 2003, Steffen et al. 2003, Ueda et al. 2003, Brusa et al. 2003, Perola et al. 2004 and Barger et al. 2005 for similar results and discussions. See also §4.6).

As Figure 4 shows, there is no evidence of a dependence on redshift of the distribution of AGN1 and AGN2 as a function of L_X and N_{H0} . We have thus estimated the probability of an AGN to appear as an AGN1 as a function of L_X and N_{H0} only, by assuming no dependence on redshift. This probability has been estimated as a function of L_X in two bins of N_{H0}^{10} : at $N_{H0} \leq 10^{21.5} \text{ cm}^{-2}$

¹⁰ We chose to use, here, the observed column densities (N_{H0}) instead of the intrinsic ones (N_H) in order to eliminate the dependencies on the redshift. A constant (with z) $N_{H0} = 10^{21.5} \text{ cm}^{-2}$ separation limit corresponds to a shifts of this limit towards higher values of N_H with increasing redshift (as the intrinsic and the $z=0$ column densities are related by the equation $\log(N_H) = \log(N_{H0}) + 2.42 \log(1+z)$). We will come back to this point in the next Sections. However, we wish to stress here that the above relationships have been derived only in order to correct the

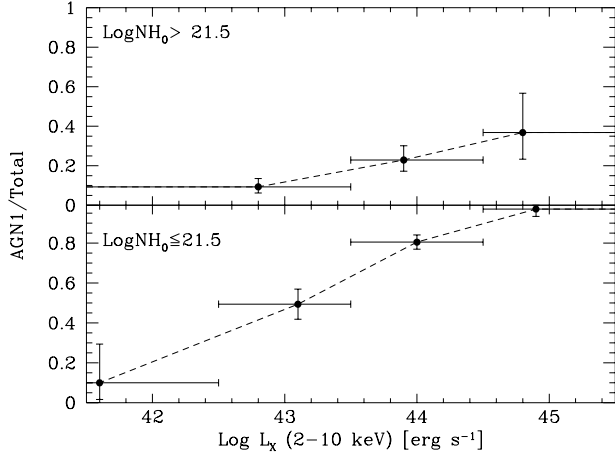


FIG. 5.— Fraction of optical type 1 AGN with $N_{H0} > 10^{21.5} \text{ cm}^{-2}$ (up), and $N_{H0} \leq 10^{21.5} \text{ cm}^{-2}$ (bottom) as function of the intrinsic luminosity L_X .

and $N_{H0} > 10^{21.5} \text{ cm}^{-2}$. The values of the probability of an AGN to appear as an AGN1 in these two N_{H0} intervals are shown in Figure 5.

We caution the reader that, due to inhomogeneities on the quality of the spectroscopic classification of the samples used, the above measure of the fraction of AGN1 as a function of L_X and N_{H0} has uncertainties that are difficult to quantify. However, these estimates are only used to derive which fractions of the unidentified AGN will follow the two L_X - L_R relationships shown in eq. 4 and 5. The absence of many outliers in the L_X - L_R relationships for AGN1 and AGN2 shown in Figure 3, demonstrates qualitatively that classification errors should not be very large. This, in principle, does not imply that more accurate spectroscopy would not change the optical classification of the AGN, but that the spectroscopy is accurate enough, for our purposes, to decide which of the two L_X - L_R relationships the AGN would follow. However, the completeness correction is computed under the assumption that the measured fraction of AGN1 as a function of L_X and N_{H0} and the derived two L_X - L_R relationships for AGN1 and AGN2 hold also for the higher redshift, optically fainter, unidentified population. We will discuss in §4 how much the uncertainties on these assumptions would affect our results.

In summary, the completeness function $g(L_X, z, N_H, R_i)$ was computed as follows: for each given AGN having intrinsic luminosity L_X , redshift z , and absorption column-density N_H , a) the N_{H0} was derived according to the equation $\text{Log}(N_{H0}) = \text{Log}(N_H) - 2.42\text{Log}(1+z)$, b) the probabilities to be an AGN1 (Q1) and AGN2 (1-Q1) were estimated according to the values plotted in Figure 5, and then c) according to eq. 4 and 5 *and their spreads*, the two probabilities (for the fraction of AGN1 and AGN2) to be brighter than the spectroscopic limit R_i of the i th sample were computed and summed.

samples for spectroscopic incompleteness, and that $N_{H0} = 10^{21.5} \text{ cm}^{-2}$ should not be meant as the working separation limit between absorbed and un-absorbed AGN, which (as defined in §1) instead is $N_H = 10^{22} \text{ cm}^{-2}$.

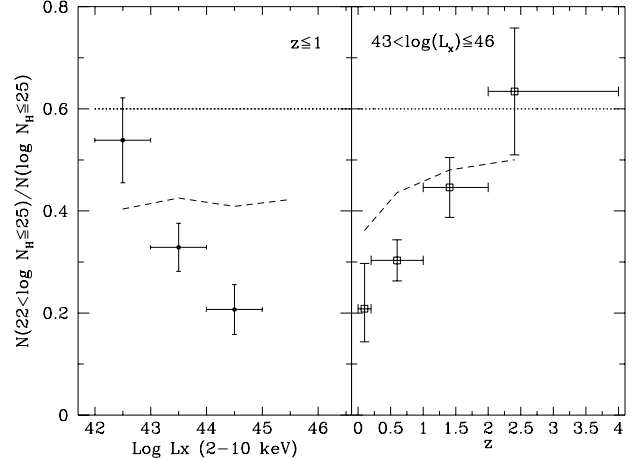


FIG. 6.— Observed fraction of absorbed ($N_H > 10^{22} \text{ cm}^{-2}$) AGN as a function of L_X (left panel) and z (right panel). The dotted lines are the intrinsic fractions assuming a constant flat N_H distribution in the range $10^{20} < N_H < 10^{25} \text{ cm}^{-2}$. The dashed lines are the expectations taking into account the selection effects.

3.4. The N_H function

To describe the distribution of the spectral parameters of the AGNs at a given luminosity and redshift, we introduced the N_H function, $f(L_X, z; N_H)$, a probability-distribution function for the absorption column-density as a function of L_X and z . The N_H function (in $\text{Log} N_H^{-1}$ units) is normalized to unity at each redshift, over the N_H interval $20 < \text{Log} N_H < 25$:

$$\int_{20}^{25} f(L_X, z; N_H) d\text{Log} N_H = 1. \quad (6)$$

The objects have been grouped into 5 bins of N_H , $\Delta \text{Log} N_H = 1$ wide, and centered at $\text{Log} N_H = 20.5, 21.5, 22.5, 23.5, 24.5$. The first bin includes all the AGNs having $N_H < 10^{21} \text{ cm}^{-2}$.

In Figure 6 the observed fraction of absorbed ($N_H > 10^{22} \text{ cm}^{-2}$) AGN as a function of L_X and z is shown. The dotted lines correspond to the fraction of absorbed objects if a flat N_H distribution in the range $10^{20} < N_H < 10^{25} \text{ cm}^{-2}$ were assumed, with no selection effects taken into account. The dashed lines show our predictions when these effects are included. Such a model does not provide a good fit to the data points, where a decrease with the intrinsic luminosity and an increase with the redshift is observed. This behavior is also evident in Figure 7. Bearing in mind that the N_H estimates are affected by uncertainties that can be as large as one decade, from the analysis of Figure 7 it appears that the assumption of a flat N_H distribution produces an expected distribution roughly in agreement with the observed one at $N_H > 10^{21} \text{ cm}^{-2}$. Hence, the observed change of the fraction of absorbed AGN as a function of L_X and z (see Figure 6), could be mainly attributed to a change of the fraction of AGN with $N_H < 10^{21} \text{ cm}^{-2}$. This will be our working hypothesis, which we will analyze in the next Sections.

We have thus assumed a flat N_H distribution between $N_H = 10^{21} \text{ cm}^{-2}$ and $N_H = 10^{25} \text{ cm}^{-2}$, while allowing the fraction of objects with $N_H < 10^{21} \text{ cm}^{-2}$ to vary. We in-

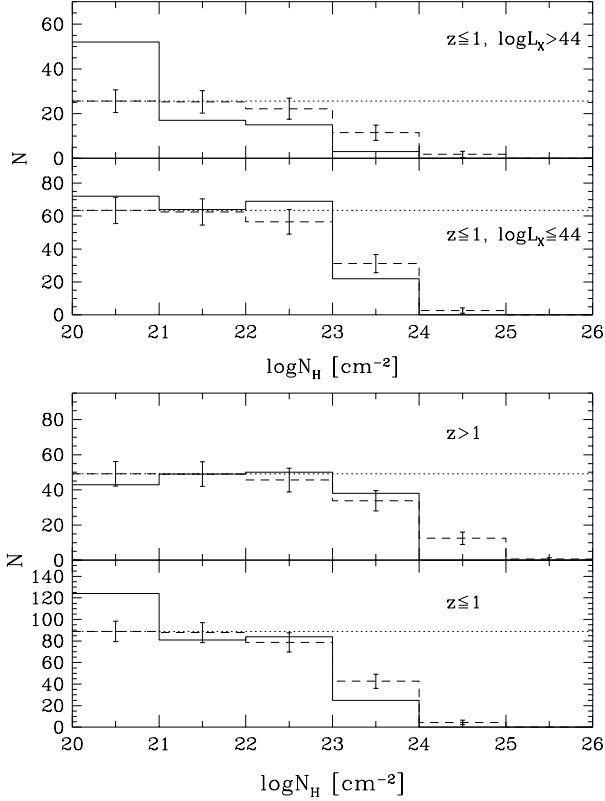


FIG. 7.— N_H distributions in various luminosity and redshift intervals. *Top.* High luminosity and low luminosity AGN at $z < 1$. *Bottom.* High and low redshift AGN. The continuous lines are the observed distributions, the dotted lines are the assumed (constant flat) N_H distributions, while the dashed lines are the expectations taking into account the selection effects.

roduced a linear dependence of the fraction of objects with $N_H < 10^{21} \text{ cm}^{-2}$ ($\Psi = f(L_X, z; \text{Log} N_H < 21)$) on both $\text{Log} L_X$ and z :

$$\Psi(L_X, z) = \psi[(\text{Log} L_X - 44)\beta_L + 1][(z - 0.5)\beta_z + 1], \quad (7)$$

where ψ is the fraction of objects with $N_H < 10^{21} \text{ cm}^{-2}$ at $L_X = 10^{44} \text{ erg s}^{-1}$ and $z = 0.5$, and β_L and β_z are the slopes of the linear dependences on L_X and z respectively. This choice is the simplest possible according to the quality of the data. The function holds for the ranges $0.25 \leq z \leq 2.75$ and $10^{42.5} \leq L_X \leq 10^{45.5} \text{ erg s}^{-1}$. At redshifts and luminosities outside these ranges the fraction was kept constant, equal to the values assumed at the limits of the ranges. Obviously Ψ could take all values in the range $[0, 1]$. This corresponds to an allowed fraction of absorbed objects ($N_H > 10^{22} \text{ cm}^{-2}$) in the range 0% - 75%. Indeed, according to eq. 6 and the assumption of a flat N_H distribution at $N_H > 10^{21} \text{ cm}^{-2}$, the fraction of absorbed AGN turns out to be:

$$\frac{N(22 < \text{Log} N_H \leq 25)}{N(\text{Log} N_H \leq 25)} = 0.75(1 - \Psi). \quad (8)$$

As clear from Figure 7, no object with $N_H > 10^{25} \text{ cm}^{-2}$ is either expected or observed. Thus, we limited our statistical analysis of the evolution of the AGN to the

objects having $N_H \leq 10^{25} \text{ cm}^{-2}$ (see eq. 6). However, when we will predict the number counts, X-ray background and the accretion history (§4.3, §4.4 and §5.2), we will include in the N_H distribution a number of objects with $10^{25} < N_H \leq 10^{26} \text{ cm}^{-2}$, equal to that in the interval $10^{24} < N_H \leq 10^{25}$.

3.5. χ^2 fitting

In order to find the best fitting model we choose two χ^2 estimators as figure of merit functions.

The first estimator (χ_{LF}^2) is related to the shape and evolution of the HXLF and is obtained by comparing the expected and observed numbers of AGN in 24 bins, covering the whole sampled Hubble space ($L_X - z$; see Figure 8 for an example of the binning). Computations have been carried out in the $0 < z < 4.5$ redshift range, and in the $10^{42} < L_X < 10^{47} \text{ erg s}^{-1}$ luminosity range. A total of 508 AGN were used. 190 had the N_H column densities directly measured from X-ray spectroscopic analysis.

The second estimator (χ_{NH}^2) is related to the N_H function, $f(L_X, z; N_H)$, i.e. the shape of the N_H distribution and its dependence on L_X and z . One contingency table was created dividing the objects with column densities higher or lower than $N_H = 10^{22} \text{ cm}^{-2}$ into 5 further bins in the $L_X - z$ space. The χ_{NH}^2 estimator was computed by comparing the expected and observed number of AGN in the total 10 (2×5) bins.

The reasons for using two different χ^2 estimators are: a) the number of objects is too small to construct a single χ^2 estimator using bins in the three-dimensional space $L_X - z - N_H$; b) the two χ^2 estimators cannot be summed as the data used are not independent. The shape and the evolution of the HXLF is only marginally dependent on the shape and evolution of the N_H distribution (we checked that the best fit parameters of the HXLF vary within the 1σ uncertainties when the parameters of the N_H distribution are left to vary within a 3σ range of their best-fit values).

The final fit was obtained by iteratively searching for the lowest values of χ_{LF}^2 and χ_{NH}^2 in turn, until the changes on the two χ^2 estimators were smaller than 0.1^{11} . For each model the probabilities for χ_{LF}^2 and χ_{NH}^2 , according to the corresponding degrees of freedom, were computed. Confidence regions of each parameter have been obtained by computing $\Delta\chi^2$ at a number of values around the best fit solution, while letting the other parameters free to float (see Lampton et al. 1976). The 68% confidence regions quoted correspond to $\Delta\chi^2 = 1.0$. Moreover, in order to use an un-binned goodness of fit test of the HXLF models, we used also a bi-dimensional Kolmogorov-Smirnov test (2D-KS, Fasano & Franceschini 1987) on the Hubble ($L_X - z$) space.

4. RESULTS

4.1. The LDDE model

By introducing the evolution factor

$$e(z) = \begin{cases} (1+z)^{p1} & (z \leq z_c) \\ e(z_c)[(1+z)/(1+z_c)]^{p2} & (z > z_c), \end{cases} \quad (9)$$

¹¹ This is a small enough interval, as the variance on the χ^2 estimator is $2N_d$, where N_d are the degrees of freedom. Variations of $\Delta\chi^2 = 0.1$ correspond to confidence levels of less than 2% and 3% for χ_{LF}^2 and χ_{NH}^2 respectively.

TABLE 2
2-10 KEV AGN LF PARAMETERS

Model	A ^a	$p1$	$p2$	z_{cut}	α	$\text{Log}L_a$ ^b	$\text{Log}L^*$ ^b	γ_1	γ_2	ψ	β_L	β_z	$P_{LF}(\chi^2)^c$	$P_{LF}(KS)^c$	$P_{N_H}(\chi^2)^c$	XRB_{2-10}^d
LDDE																
1	1.48	4.37	-1.19	2.39	0.20	45.74	44.26	0.94	2.35	0.26	0.00	-0.00	20	6	0.07	1.76
2	1.50	4.39	-1.14	2.41	0.20	45.74	44.25	0.97	2.36	0.29	0.43	-0.00	20	6	0.5	1.78
3	1.39	4.48	-1.19	2.39	0.20	45.74	44.26	0.94	2.35	0.30	0.00	-0.33	19	5	0.09	1.75
4	1.21	4.62	-1.15	2.49	0.20	45.74	44.25	1.01	2.38	0.44	0.62	-0.51	20	7	83	1.81
5 ^e	1.29	4.85	-1.03	2.45	0.22	45.73	44.23	1.09	2.44	0.36	0.67	-0.00	33	21	20	2.16
Errors 5%		+0.26 -0.26	+0.72 -0.68	+0.82 -0.68	+0.04 -0.03	+0.58 -0.63	+0.18 -0.18	+0.08 -0.10	+0.13 -0.11	+0.04 -0.05	+0.14 -0.13	+0.14 -0.17				
LDDE																
6	6.18	3.22	...	1.08	43.79	0.95	2.74	0.46	0.64	-0.58	9	3	63	2.54
Errors 5%		+0.13 -0.26	...	+0.08 -0.06	+0.15 -0.11	+0.06 -0.07	+0.27 -0.23	+0.04 -0.05	+0.14 -0.13	+0.14 -0.17				

^aIn units of $10^{-6} h_{70}^3 \text{ Mpc}^{-3}$.

^bIn units of erg s^{-1} .

^cProbability values in % units.

^dIn units $10^{-11} \text{ erg cm}^{-2} \text{ s}^{-1} \text{ deg}^{-2}$.

^eOnly Piccinotti, AMSSn and CDF-N samples used.

the pure density evolution (PDE) model is expressed as

$$\frac{d\Phi(L_X, z)}{d\text{Log}L_X} = \frac{d\Phi(L_X, 0)}{d\text{Log}L_X} e(z). \quad (10)$$

The z_c parameter represents the redshift at which the evolution stops. $p1$ is the parameter characterizing the rate of the evolution, while $p2$ is usually negative and characterizes the rate of the counter-evolution of the HXLF at $z > z_c$.

The LDDE model is obtained by introducing in the PDE model a luminosity dependence of z_c , assumed to be a power law:

$$z_c(L_X) = \begin{cases} z_c^* & (L_X \geq L_a) \\ z_c^* (L_X/L_a)^\alpha & (L_X < L_a). \end{cases} \quad (11)$$

The above parameterization has been introduced by Ueda et al. (2003) in order to allow for a change with luminosity of the redshift at which the density of AGNs peaks (see also Miyaji et al. 2000 for a similar LDDE parameterization). This behavior is also apparent in our data (see, e.g. Figure 8).

In order to plot the HXLF we adopted the “ $N^{\text{obs}}/N^{\text{mdl}}$ method” (La Franca & Cristiani 1997), where the best-fit model multiplied by the ratio between the number of observed sources and that of the model prediction in each L_X - z bin is plotted. Although model dependent (especially when large bins are used), this technique is the most free from possible biases, compared with other methods such as the conventional $1/V_a$ method. The attached errors are estimated from Poissonian fluctuations (1σ) in the observed number of sources according to the Gehrels (1986) formulae.

We simultaneously fitted the parameters of the HXLF and of the possible dependencies of the N_H distribution on L_X and z . As shown in Table 2, the LDDE model provides a good fit to the data regardless of the adopted N_H distribution (see Figures 8 and 9).

According to these fits, the redshift of the density peak of AGN increases with the luminosity, from $z \sim 0.5$ at

$L_X \sim 10^{42} \text{ erg s}^{-1}$ up to $z \sim 2.5$ at $L_X \sim 10^{46} \text{ erg s}^{-1}$. Out of the four proposed N_H distributions only fit # 4, provides a good fit to the whole data in the L_X - z - N_H space. The first model (fit # 1) searched for a constant value of the fraction of objects with $N_H < 10^{21} \text{ cm}^{-2}$ ($\Psi(L_X, z) = \psi = \text{constant}$, $\beta_L = \beta_z = 0$). The χ^2 probabilities of the dependence of the N_H distributions on L_X and z reject, at more than 99.93% confidence level, this model. As can be seen in Figures 6 and 7, the data requires a decrease of

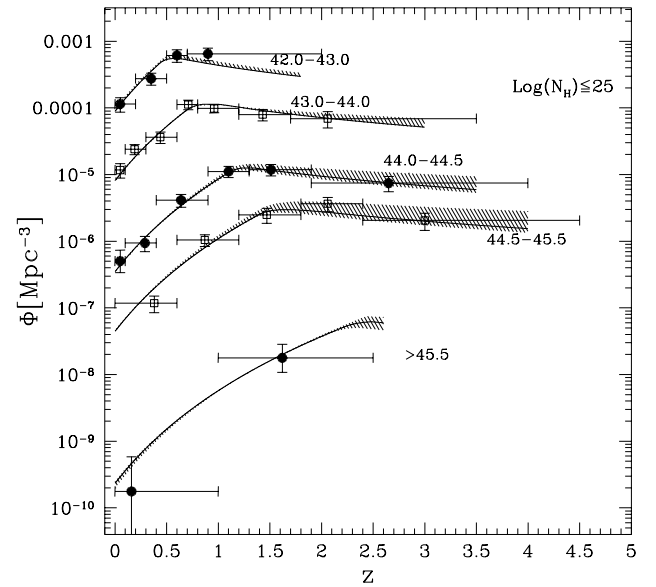


FIG. 8.— Density of AGN in luminosity bins as a function of redshift. The continuous lines are the best fit values of the LDDE model with an evolving N_H distribution depending on L_X and z (fit #4 in Table 2). Data have been plotted using the “ $N^{\text{obs}}/N^{\text{mdl}}$ method” (see §4.1). The dashed areas are the largest allowed regions due to uncertainties in the completeness correction method used (see §4.1.1).

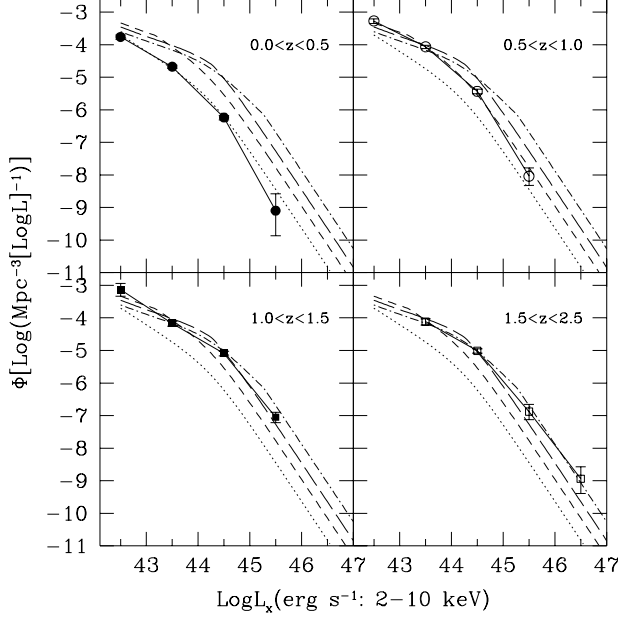


FIG. 9.— Density of AGN as a function of luminosity in four redshift intervals. The values are plotted at the central redshift of the intervals. The dashed lines are the best fit densities of the LDDE model with an evolving N_H distribution depending on L_X and z (fit #4 in Table 2). Data have been plotted using the “ $N_{\text{obs}}/N_{\text{mdl}}$ method” (see §4.1).

the fraction of absorbed objects with luminosity, and an increase with redshift. Both N_H distributions in which we allowed for a dependence of the absorbed objects on redshift or luminosity only (fits #2 and #3) are rejected at more than 99.5% confidence level. On the contrary, model #4 (Figures 8 and 9), where both a dependence on redshift and luminosity is allowed (see Figures 10 and 11), provides a very good representation of the data with a $\chi^2_{N_H}$ probability of 83%.

4.1.1. Analysis of the uncertainties and systematic biases

We analyzed how much our results could be affected by uncertainties in the completeness correction method used. These uncertainties could be introduced by errors in the spectroscopic classification of the AGN, and by the assumption that the measured fraction of AGN1 as a function of L_X and N_{H0} and the derived two L_X – L_R relationships for AGN1 and AGN2 (see §3.3) hold also for the higher redshift, optically fainter, unidentified population. In order to measure the maximum allowed range of the HXLF parameters due to uncertainties in these assumptions, we have carried out the HXLF fits under the two very extreme hypotheses that all the unidentified AGN would follow either the L_X – L_R relationship typical of the AGN1 (eq. 4), or the L_X – L_R relationship typical of the AGN2 (eq. 5). It resulted that the best-fit parameters changed within the measured 1σ uncertainties. The results are shown in Figure 8, where the largest allowed AGN density regions due to the uncertainties introduced by the completeness correction method used are shown by dashed areas.

About 60% of the AGN used in our analysis have their

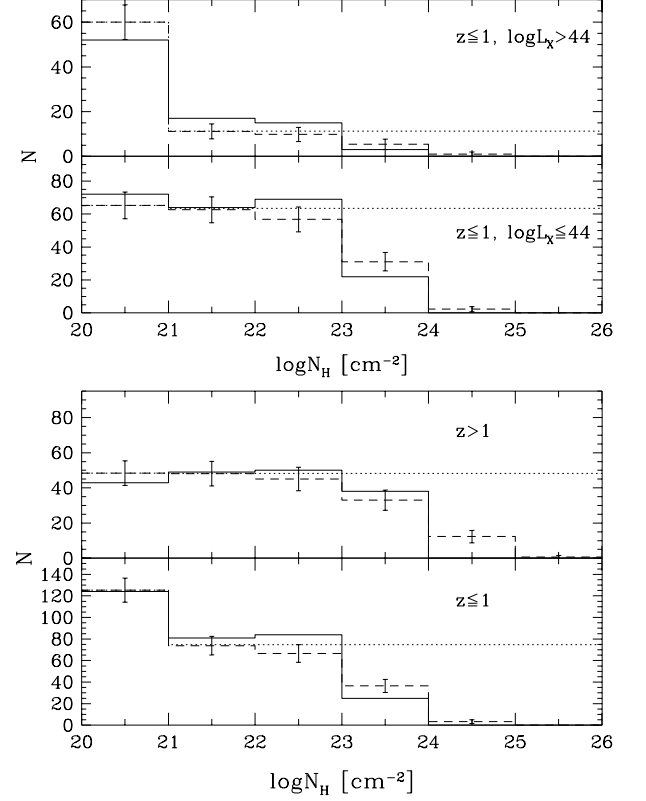


FIG. 10.— N_H distributions in various luminosity and redshift intervals. *Top.* High luminosity and low luminosity AGN at $z < 1$. *Bottom.* High and low redshift AGN. The continuous lines are the observed distributions, the dotted lines are the assumed N_H distributions (fit #4 in Table 2: evolving N_H distribution with a LDDE HXLF evolution), while the dashed lines are the expectations taking into account the selection effects.

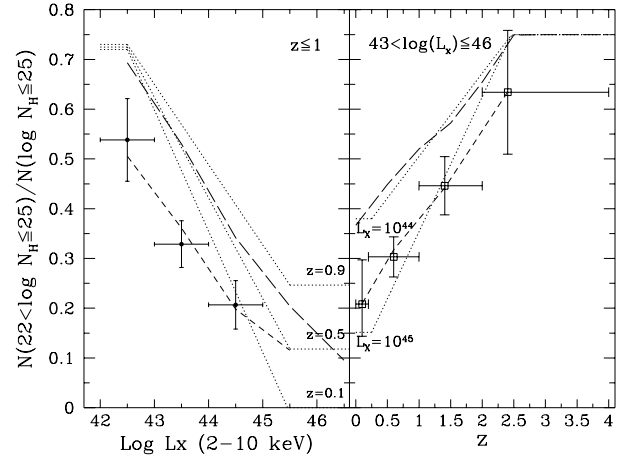


FIG. 11.— Observed fraction of absorbed ($N_H > 10^{22} \text{ cm}^{-2}$) AGN as a function of L_X and z . The dotted lines are examples of the intrinsic assumed distributions at various luminosities and redshifts (LDDE model, fit #4 in Table 2). The long dashed lines are the corresponding average intrinsic assumed distributions of the sample used. The short dashed lines are the expectations taking into account the selection effects.

N_{H} column densities derived from the hardness ratios (those belonging to the AMSSn, H2XMM0.5, CDF-N and CDF-S samples). This method could introduce some systematic bias. For example, our simple absorbed power law model could tendentially underestimate the real column densities, because scattered X-rays and circum-nuclear starburst X-rays can provide additional flux. This effect is expected to be stronger at lower luminosities where the fraction of the light coming directly from the nucleus should be smaller. If this is the case, the observed decrease of the fraction of absorbed AGN with the intrinsic luminosity should be even stronger. It should be noted, however, that Perola et al. (2004) found a rather satisfactory correlation between the column densities measured from the hardness ratios and from the X-ray spectral fits in the HELLAS2XMM sample.

Recently Tozzi et al. (2005) have published N_{H} measurements on the CDF-S sample, obtained using X-ray spectral fits. We took advantage of these measures to check whether the hardness ratio method introduces some relevant systematic bias. No relevant difference or systematic trend on either luminosity or redshift was found. In a subsample of $z \leq 1.2$ AGN, using the hardness ratios we measure a fraction of 17/32 absorbed AGN with $L_{\text{X}} > 10^{43}$ erg s $^{-1}$, while Tozzi et al. (2005) find 16/32. At lower luminosities ($10^{41} < L_{\text{X}} \leq 10^{43}$ erg s $^{-1}$) we measure a fraction of 20/31 absorbed AGN ($L_{\text{X}} > 10^{43}$), while Tozzi et al. (2005) find 18/31. In a subsample with $10^{43} < L_{\text{X}} \leq 10^{45}$ erg s $^{-1}$ at redshift below 1.5 we measure a fraction 23/43 absorbed AGN, while Tozzi et al. (2005) find 24/43. At redshift above 1.5 we find a fraction 31/43 absorbed AGN, while Tozzi et al. (2005) find 34/43.

We also checked whether our results might depend on the assumed X-ray K-correction (see §3.2). We repeated the fit # 4 assuming $\Gamma = 1.7$ or $\Gamma = 1.9$, or assuming an exponential cutoff at energy $E_{\text{C}} = 300$ keV. It turned out that the changes of the parameters are within the 1σ uncertainties.

4.2. PLE model

We also checked if a simpler pure luminosity evolution model were consistent with the data. By introducing the evolution factor

$$e(z) = \begin{cases} (1+z)^{p1} & (z \leq z_c) \\ e(z_c) & (z > z_c), \end{cases} \quad (12)$$

the PLE model is expressed as

$$\frac{d\Phi(L_{\text{X}}, z)}{d\text{Log}L_{\text{X}}} = \frac{d\Phi(L_{\text{X}}/e(z), 0)}{d\text{Log}L_{\text{X}}}. \quad (13)$$

The PLE fit (Figure 12 and fit # 6 in Table 2) provides a less probable solution for the HXLF. Furthermore the PLE fit finds that the evolution stops at $z_c = 1.08^{+0.08}_{-0.06}$. This low value should be attributed to the fact that there is an increase with luminosity of the redshift peak of the density of AGN. Low luminosity ($L_{\text{X}} < 10^{43}$ erg s $^{-1}$) AGNs peak at $z = 0.5$, while high luminosity ($L_{\text{X}} > 10^{46}$ erg s $^{-1}$) AGNs peak at $z \sim 2$. In this framework the PLE fit finds a *weighted mean* of the different redshift cut off values of the low and high luminosity AGNs.

Although formally acceptable, $z_c = 1.08^{+0.08}_{-0.06}$ is significantly smaller than the previous estimates for the evolution of AGN1 in the hard X-rays ($z_c = 2.4 \pm 0.5$; La

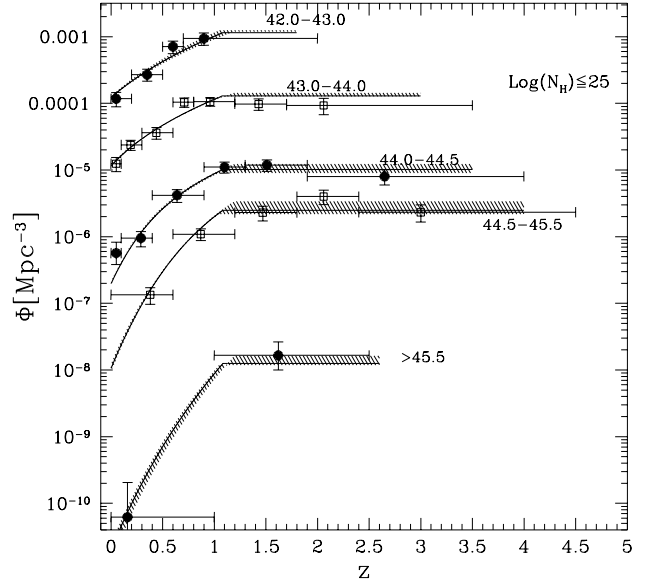


FIG. 12.— Density of AGN in luminosity bins as a function of redshift. The dashed lines are the best fit values of the PLE model with an evolving N_{H} distribution (fit #7 in Table 2). Data have been plotted using the “ $N^{\text{obs}}/N^{\text{mdl}}$ ” method” (see §4.1). The dashed areas are the largest allowed regions due to uncertainties in the completeness correction method used (see §4.1.1).

Franca et al. 2002), and in the optical band ($z_c \sim 2.0$; see e.g. Boyle et al. 2000). This difference should be attributed to the fact that both the hard X-ray AGN1 and the optical QSO populate preferentially the bright part of the HXLF (see e.g. Figure 5 and related discussion) which, also in the LDDE model, faces a redshift cut off larger than 1.5–2. If the fit of the PLE model is carried out with a fixed $z_c = 2.0$, it turns out unacceptable, with a χ^2_{LF} probability of $3.4 \times 10^{-6}\%$ and a 2D-KS probability of 0.27%. On the basis of these results and on the fact that the PLE model over-predicts the 2–10 keV X-ray background (XRB, see Table 2) and the soft X-ray counts (see §4.3), we consider such a parameterization of the HXLF evolution to be ruled out.

4.3. The Counts

Down to the flux limit adopted in this analysis (10^{-15} erg cm $^{-2}$ s $^{-1}$), the 2–10 keV counts predicted by the models described in Table 2 are in good agreement with both the counts of the whole sample (including the objects without spectroscopic identifications), and with the Bauer et al. (2004) compilation (see Figure 13). The fit of Moretti et al. (2003) is also shown. This is an *a posteriori* test implying that our method, used to correct for the spectroscopic incompleteness of the faint samples, is reliable. At faint fluxes ($S < 10^{-15}$ erg cm $^{-2}$ s $^{-1}$, where there are no data in our samples) the LDDE model is consistent within the errors with the data, while the PLE model tends to over-predict the measured number density¹². This is mainly due to a higher density of low

¹² As explained in §3.4, we have included in the N_{H} distribution a fraction of objects with $10^{25} < N_{\text{H}} \leq 10^{26}$ cm $^{-2}$, equal to that in the interval $10^{24} < N_{\text{H}} \leq 10^{25}$.

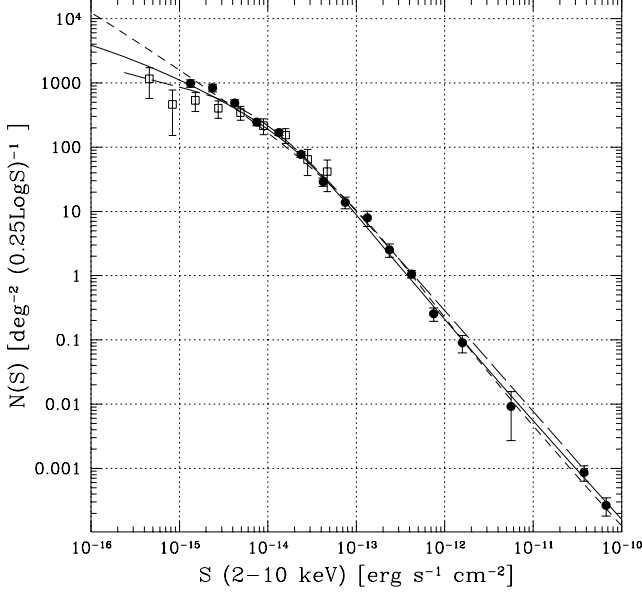


FIG. 13.— Differential counts of AGN in the 2–10 keV band. The filled circles are our estimates from the samples used in this analysis. The open squares are the estimates from Bauer et al. (2004). The continuous line are the counts predicted by the LDDE model (fit # 4), while the short dashed line are the counts of the PLE model (fit # 6). The long dashed line are the estimates from a compilation of Moretti et al. (2003).

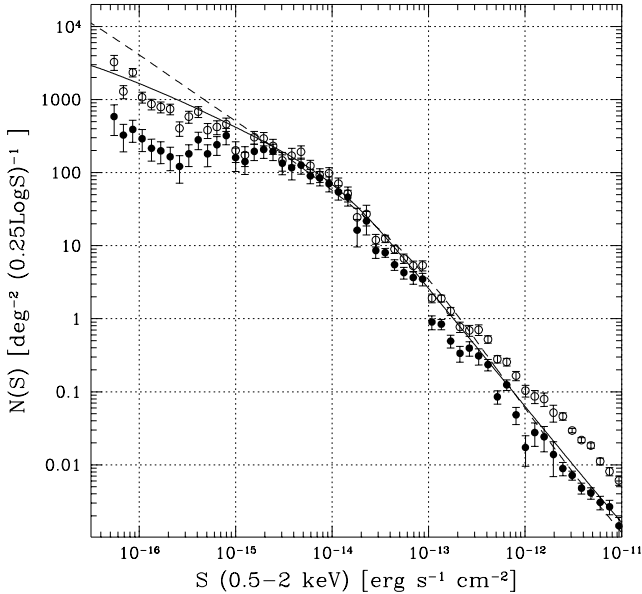


FIG. 14.— Differential counts of X-ray sources in the 0.5–2 keV band (open squares) and of AGN-1 (filled squares) from a compilation of Hasinger et al. (2005). The continuous line are the counts predicted by the LDDE model (fit # 4), while the dashed line are the counts of the PLE model (fit # 6).

luminosity AGNs in the HXLF (in comparison with the LDDE model), and to the absence of a counter-evolution at high redshift in the PLE model.

Although this analysis is based on observations made

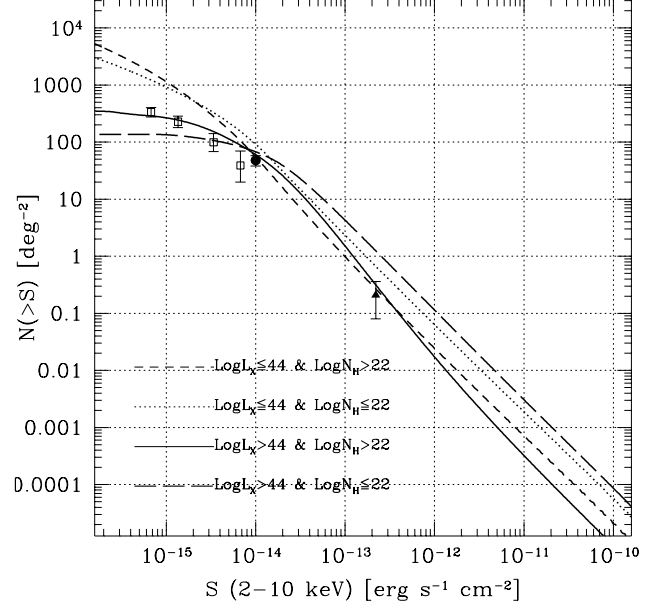


FIG. 15.— Predicted counts (from our best-fit LDDE model #4) of AGN for un-absorbed and absorbed AGN divided into two luminosity classes. The filled dot is the measure of the density of QSO2 by Perola et al. (2004), the open circles are the density of QSO2 derived by Padovani et al. (2004), while the triangle is the measure of the density of QSO2 from the HBS28 sample of Caccianiga et al. (2004).

in the 2–10 keV band, it is instructive to compare our results with the 0.5–2 keV counts. Of course, we should be aware that, when predicting the 0.5–2 keV counts, our results depend on the spectral assumptions (a $\Gamma=1.8$ spectral slope plus photoelectric absorption), which could not be valid below 2 keV. The PLE model over-predicts the observed soft counts as compiled by Hasinger et al. (2005) at faint ($S < 10^{-15}$ erg cm $^{-2}$ s $^{-1}$) fluxes (see Figure 14). The situation is even worse, since at faint fluxes we expect a relevant contribution from normal X-ray galaxies to the counts (about 20 deg $^{-2}$ and 400 deg $^{-2}$ at $S_{0.5-2}=10^{-15}$ erg cm $^{-2}$ s $^{-1}$ and $S_{0.5-2}=10^{-16}$ erg cm $^{-2}$ s $^{-1}$ respectively; Ranalli et al. 2003, Bauer et al. 2004). On the contrary, the LDDE model provides a more acceptable solution. At bright fluxes the observed counts are above our predictions because the X-ray sources are dominated by stars and clusters of galaxies which are not included in our models.

4.3.1. The density of absorbed AGN

The 2–10 keV predicted counts obtained from the best fit model for the HXLF (# 4) are shown in Figure 15, after being splitted according to X-ray absorption and X-ray luminosity. Most of the luminous ($L_X > 10^{44}$ erg s $^{-1}$), absorbed ($N_H > 10^{22}$ cm $^{-2}$) sources are AGN2 (see also the discussion in §3.3). Luminous, obscured AGN are usually referred to as QSO2 and in the simplest version of the AGN unified scheme are predicted to be more numerous than QSO1 by a factor comparable to that observed for lower luminosity Seyfert galaxies (about 3–4). Despite extensive searches, narrow-line optically luminous QSO2 appear to be extremely rare and by far less numerous than broad line quasars (see Halpern, Er-

acleous & Forster 1998 and references therein). Because of the selection effects due to obscuration, X-ray surveys are expected to provide an unbiased census of the QSO2 population and a more reliable estimate of their space density. Several QSO2 candidates (i.e. luminous, X-ray obscured sources) have been discovered by *Chandra* and XMM-*Newton* surveys (~ 20 in the HELLAS2XMM survey, Fiore et al. 2003, Mignoli et al. 2004, Cocchia et al. 2005; ~ 30 in the CDF-S+CDF-N; a dozen in the CLASXS survey, Barger et al. 2005). A sizable fraction of them (from 50% to 75%) has been confirmed by deep optical spectroscopic observations. A notable example has been reported by Norman et al. (2002). It should be noted that the quality of spectroscopic observations is not uniform and, given the relatively high redshifts, the $H\alpha$ and $H\beta$ wavelengths are poorly sampled, thus hampering a “pure” optical classification. On the other hand, it is important to remind that the QSO2 classification is wavelength dependent. Several, X-ray obscured, luminous QSO2 do not show any evidence of strong emission lines even in high quality optical spectra, among them the QSO2 prototype NGC 6240 (Vignati et al. 1999). Keeping in mind these caveats, and adopting an admittedly arbitrary luminosity threshold ($L_X > 10^{44}$ erg s $^{-1}$), we obtain a QSO2 space density of 60 and 267 deg $^{-2}$ at 2–10 keV fluxes brighter than 10^{-14} and 10^{-15} erg cm $^{-2}$ s $^{-1}$ respectively. The slope of the integral counts significantly flattens below 10^{-14} erg cm $^{-2}$ s $^{-1}$. As a consequence, the QSO2 surface density at fluxes much fainter than those actually probed (i.e. 10^{-16} erg cm $^{-2}$ s $^{-1}$) increases by a relatively small amount reaching 354 deg $^{-2}$. These figures have at least a 5% error, corresponding to the HXLF normalization uncertainties. The predicted counts (Figure 15) are in good agreement with the QSO2 space densities measured by Caccianiga et al. (2004), Perola et al. (2004) and Padovani et al. (2004).

4.4. The XRB spectrum: a self-consistency check

A detailed modeling of the XRB spectrum over the full ~ 2 –400 keV range is beyond the scope of this paper. Nevertheless, it is important to check that the evolving X-ray luminosity function and the N_H distribution derived in the previous sections match the XRB flux at least in the 2–10 keV energy range. To this end it is useful to remind that the XRB intensity below ~ 10 keV, as measured by several imaging X-ray telescopes, is likely to be affected by systematic errors. In Figure 16 a compilation of XRB measurements is reported. The maximum difference is of the order of 30% between the EPIC-*pn* flux reported by De Luca & Molendi (2004) and the *HEAO1*-A2 measure of Marshall et al. (1980). According to a recent reanalysis of the *HEAO1*-A2 data (Revnitsev et al. 2004) the 3–60 keV spectrum should be renormalized upward by about 15%. The resulting 2–10 keV flux is 1.96 ± 0.10 erg cm $^{-2}$ s $^{-1}$ deg $^{-2}$. The solid curve in Figure 16 represents the integrated AGN spectrum obtained with our best fit LDDE model for the HXLF (fit # 4) with the redshift and luminosity dependent N_H function¹³. Our predicted 2–10 keV flux of 1.81×10^{-11} erg cm $^{-2}$ s $^{-1}$ deg $^{-2}$ corresponds to $\sim 92\%$ of the Revnitsv

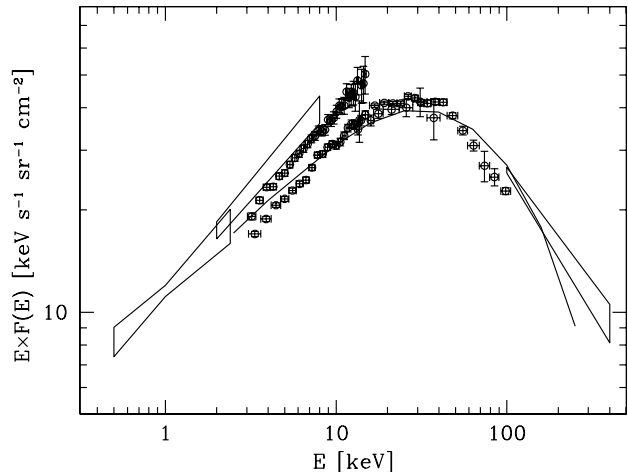


FIG. 16.— Integrated AGN spectrum computed from the best fit LDDE model for the HXLF (fit # 4) with the redshift and luminosity dependent N_H function. The model predictions are compared with a selection of XRB spectral measurements over the broad 0.5–400 keV energy range. The regions enclosed within the bow-ties correspond to the XRB spectrum and associated errors as measured by ROSAT (Georgantopoulos et al. 1996) in the 0.5–2 keV band and by XMM-*Newton* (De Luca & Molendi 2004) in the 2–8 keV band. The data points in the 3–15 keV energy range are from *RXTE* (Revnitsev et al. 2003), while those in the 3–60 keV are from *HEAO1*-A2 (Marshall et al. 1980). The bow-tie at high energies (100–400 keV) is from *HEAO1*-A4 (Kinzer et al. 1997).

et al. (2004) value and 108% of the original *HEAO1*-A2 measure. Given that the XRB synthesis has been obtained with very simple prescriptions for the intrinsic (before absorption) spectral energy distribution (a power law spectrum with $\Gamma=1.8$ plus an exponential high energy cut-off e^{-E/E_C} with $E_C=200$ keV for all AGN) it is reassuring to obtain a reasonably good description of the XRB spectral intensity over a broad energy range. As a final remark we note that an increasing ratio between absorbed and un-absorbed AGN towards high redshifts has been already included in the synthesis models of Pompilio et al. (2000) and Gilli et al. (2001) though with different prescription for the absorption distribution.

4.5. The LF of absorbed and un-absorbed AGN

It is interesting to plot the evolution of absorbed ($N_H > 10^{22}$ cm $^{-2}$) and un-absorbed AGN, according to our best fit LDDE solution (fit # 4; Figure 17). As expected, the absorbed AGN outnumber the un-absorbed ones at low luminosities and high redshifts. In the bottom panel of Figure 17 the HXLF is compared with the estimate of Miyaji et al. (2000) of the soft X-ray (0.5–2 keV) AGN LF (a slope $\Gamma=1.8$ has been assumed to convert the 0.5–2 keV luminosities into the 2–10 keV band). It turns out that, at low redshifts ($z \sim 0.25$), the soft X-ray LF is almost coincident with our measure of un-absorbed AGN HXLF, while at high redshifts the soft X-ray LF is consistent, within the uncertainties, with the total HXLF. This behavior is explained by the stronger

¹³ As explained in §3.4, we have included in the N_H distribution a fraction of objects with $10^{25} < N_H \leq 10^{26}$ cm $^{-2}$, equal to that in the interval $10^{24} < N_H \leq 10^{25}$.

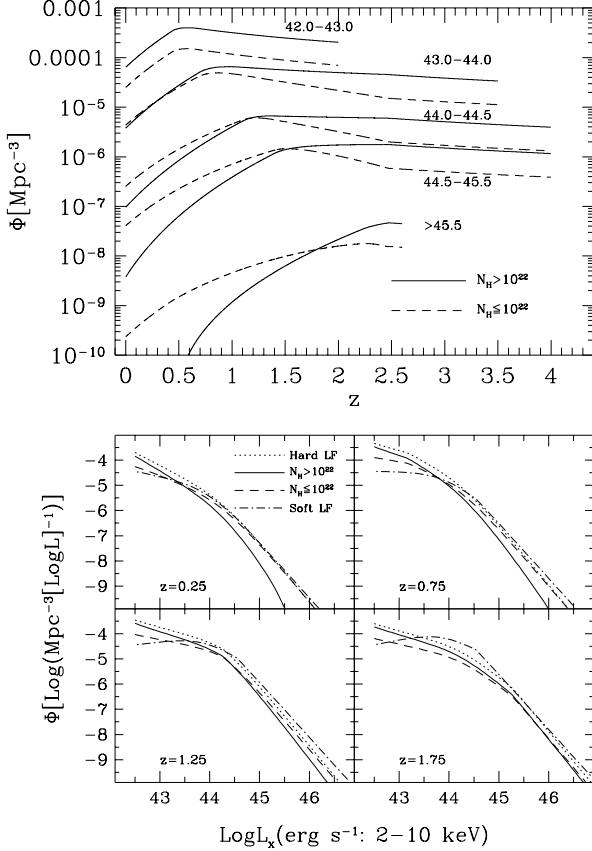


FIG. 17.— *Top*. Density of absorbed and un-absorbed AGN in luminosity bins as a function of redshift (fit # 4). *Bottom*. Density of absorbed and un-absorbed AGN as a function of luminosity in four redshift intervals (fit # 4). The dot-dashed line is the 0.5–2 keV LF of AGN of Miyaji et al. (2000; plotted assuming $\Gamma=1.8$).

effects of absorption in the soft X-rays in comparison to hard X-rays, especially at low redshifts. As a consequence, at low redshifts, only un-absorbed AGN are detected in the soft X-ray band, while at high redshifts the bias reduces, and the same population which is observed in the 2–10 keV band is detected. As a consequence, the soft X-ray LF faces a stronger (LDDE) evolution than observed for the HXLF (see Hasinger et al. 2005).

4.6. The LF of AGN1 and AGN2

The space density and evolution of AGN1 and AGN2 can be estimated using the above described method. In order to correct for the spectroscopic incompleteness of the faint samples we had to compute the *completeness function* $g(L_X, z, N_H, R)$ (see §3.3) which is based on the estimate of the probability of an AGN to appear as an AGN1 as a function of L_X , N_H and z : $Q1(L_X, z, N_H)$ (shown in Figure 5). With this estimate in hand (and keeping in mind the uncertainties on the AGN1-AGN2 optical classification discussed in §3.3), we can derive the AGN1 luminosity function:

$$\Phi_1(L_X, z) = \int \Phi(L_X, z) f(L_X, z; N_H) Q1(L_X, N_H, z) dN_H, \quad (14)$$

where, as discussed in §3.4, $f(L_X, z; N_H)$ is the N_H distribution. The AGN2 density can be derived by sub-

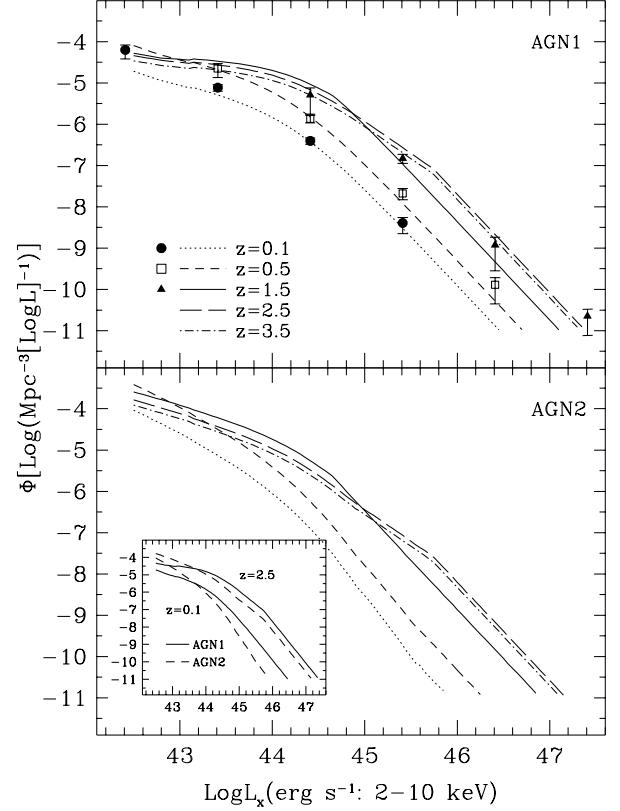


FIG. 18.— *Top*. Evolution of the luminosity function of AGN1 up to $z = 3.5$. The data are the estimates of the density of AGN1 from La Franca et al. (2002). *Bottom*. Evolution of the luminosity function of AGN2 up to $z = 3.5$. The lines have the same meaning as in the top panel. The small picture shows the difference among the luminosity functions of AGN1 and AGN2 at $z = 0.1$ and $z = 2.5$.

stituting, in the above formula (eq. 14), $Q1(L_X, N_H, z)$ with $1-Q1(L_X, N_H, z)$. As can be seen in Figure 18, at low redshifts ($z < 0.5$), the AGN2 density low luminosities ($L_X \sim 10^{42}-10^{43} \text{ erg s}^{-1}$) is about five times larger than that of AGN1, while the latter outnumber the former by an order of magnitude at high luminosities ($L_X \sim 10^{46}$). In Figure 18 the AGN1 density in the 2–10 keV band from the *BeppoSAX* HELLAS survey as computed by La Franca et al. (2002) is reported. The present estimate of the AGN1 luminosity function is consistent, within the uncertainties, with the La Franca et al. (2002) findings, thus confirming that $Q1$ is a reliable measure of the probability of an AGN to appear as an AGN1.

5. DISCUSSION

5.1. Comparison with previous results

A specific procedure to correct for the spectroscopic incompleteness of faint X-ray sources which also takes into account the selection effects due to X-ray absorption has allowed us to use a large AGN sample to compute the HXLF. Our results extend those of Cowie et al. (2003) and Barger et al. (2005), where no correction for X-ray absorption is adopted, and the upper limits to the AGN density are estimated by assigning to the unidentified sources the redshifts corresponding to the centers of each

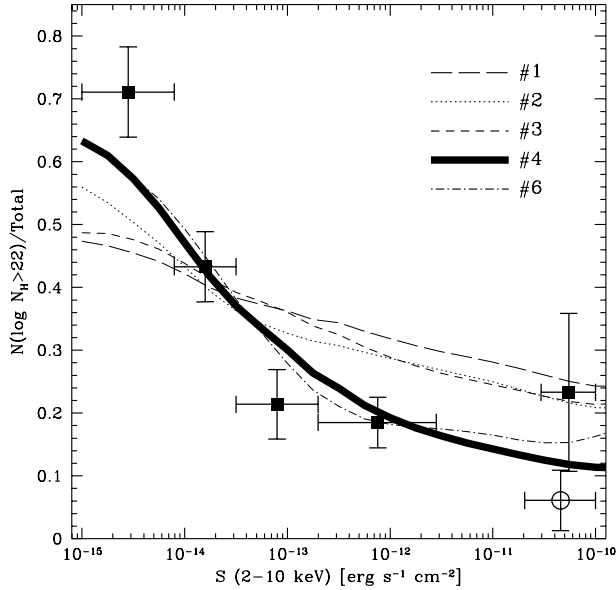


FIG. 19.— Observed fraction of absorbed AGNs as measured from the samples used in this analysis. The lines correspond to the predictions of the fitted HXLF listed in Table 2. The open circle is the value obtained from the sample of Grossan (1992; not included in the analysis of the HXLF).

L_X - z bin.

A LDDE model provides the best fit to the HXLF evolution up to $z = 4$, in agreement with the Ueda et al. (2003) findings obtained using a smaller and brighter sample, and also with the estimates of Cowie et al. (2003), Fiore et al. (2003), Hasinger et al. (2005) and Silverman et al. (2005) who found that the AGN number density for luminosities lower than $\sim 10^{44}$ erg s $^{-1}$ peaks at lower redshifts than that of higher luminosity AGN.

The new result or our analysis concerns the luminosity and redshift dependence of the fraction of absorbed AGN, which decreases with luminosity and increases with redshift. The luminosity trend was already pointed out by Ueda et al. (2003) (see also Hasinger et al. 2005). In the Ueda et al. (2003) best fit model the fraction of absorbed AGN is 57% and 36% at $L_X = 10^{42.5}$ erg s $^{-1}$ and $L_X = 10^{45}$ erg s $^{-1}$ respectively. Taking into account only a luminosity dependence on the fraction of absorbed AGN in our sample (fit # 2 in Table 2), the corresponding fractions at $L_X = 10^{42.5}$ erg s $^{-1}$ and $L_X = 10^{45}$ erg s $^{-1}$ are 68% and 40% respectively. The two results are remarkably similar, especially if we note that absorbed AGN with $24 < \text{Log } N_H < 25$ are included in our sample but not in Ueda et al. (2003).

The increase of the fraction of absorbed AGN with redshift, instead, emerges only with our analysis. The difference with respect to the Ueda et al. (2003) findings is due to the larger sample extending to fainter fluxes used in the present analysis. Indeed, if we restrict our analysis to a subsample (fit #5 in Table 2) of 207 objects from the Piccinotti, AMSSn and CDF-N catalogs and thus quantitatively similar to that used by Ueda et al. (2003) the uncertainties become so large that the redshift dependence is no longer significant while the luminosity dependence is recovered.

It is worth noting that the luminosity and redshift dependence of the absorbed AGN fraction would disappear if one flux limited sample only were analyzed (as discussed by Perola et al. 2004). A flux limited sample selects low luminosity AGN at low redshifts (which, according to our analysis, are more absorbed) and high luminosity AGN at high redshift (which are more absorbed as well!). Then the average fraction of absorbed AGN turns out to be roughly constant. Only combining several samples, and thus covering wide strips of the L_X - z plane with almost constant redshift or luminosity, it is possible to disentangle the true dependencies.

A simple AGN model based on the unified paradigm has been adopted by Treister et al. (2004). Assuming that obscured AGN outnumber unobscured ones by a factor 3 without any luminosity and/or redshift dependence they claim to be able to reproduce the observed counts, redshift and N_H distributions in the CDF-N and CDF-S samples once all the selection effects are properly taken into account. More recently Treister & Urry (2005) revised their previous analysis including a luminosity dependence of the fraction of absorbed AGN which appears to provide an equally good fit to several observational constraints. However, in both works, no comparison between the predicted and observed N_H distributions as a function of both L_X and z is made. We have repeated our analysis assuming the Treister & Urry (2005) N_H distribution (see their Fig. 1). Either using the CDF-N plus CDF-S samples only, or the full AGN sample used in this work, we found that the only statistically acceptable models are those including a dependence of the fraction of absorbed AGN as a function of L_X and z , with a behaviour similar to what measured in the present paper (see §4).

The observed and predicted fractions of absorbed ($N_H > 10^{22}$ /Total) AGN as a function of the observed flux are shown in Figure 19. The open circle is from the Grossan sample (1992; not included in this analysis¹⁴), and it is plotted in order to show the uncertainties at bright fluxes. As already described by several authors (e.g. Comastri et al. 2001; Tozzi et al. 2005; Perola et al. 2004 and references therein) the average X-ray spectrum significantly hardens towards faint fluxes and this change is mostly concentrated in the 10^{-14} – 10^{-13} erg cm $^{-2}$ s $^{-1}$ range, where the fraction of absorbed AGNs rises from about 20% to about 50%. For this reason, this measure is a very powerful tool to discriminate between different evolutionary scenarios for the N_H distribution. The only acceptable description of the observed ratio between absorbed and un-absorbed AGN as a function of the hard X-ray flux is obtained only if the ratio depends on *both* luminosity *and* redshift (fits #4 and #6 in table 2 for LDDE and PLE, respectively). These two models are indistinguishable, and in fact the fraction of absorbed AGN as a function of the X-ray flux is less sensitive to the shape and evolution of the HXLF than to the evolution of the N_H distribution (see also §3.5).

Recently, Alexander et al. (2005a, 2005b) have found evidences that a fraction of the $z > 1$ submillimeter emit-

¹⁴ A proper reassessment of the Grossan sample seems necessary before using it extensively for a detailed statistical analysis. See e.g. Bianchi et al. (2005) for a discussion on a few sources of the sample.

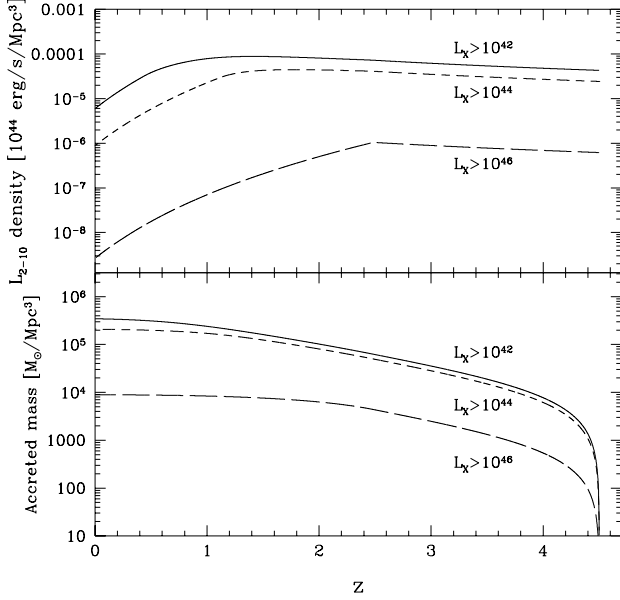


FIG. 20.— *Top.* Intrinsic (before absorption) luminosity density in the 2–10 keV band as a function of redshift from our best fit HXLF. *Bottom.* Total accreted mass as a function of redshift.

ting galaxies harbor obscured AGN. They argued that the black holes are almost continuously growing throughout vigorous star-formation episodes. These results are in agreement with the hydrodynamical simulation of galaxy mergers by Di Matteo et al. (2005) and Springel et al. (2005), where the growth of both the black holes and stellar components are taken into account. In this framework, our result of an increase of the fraction of absorbed AGN with the redshift is in agreement with a picture where the peak epoch of the star formation ($z=1-2$) corresponds to a heavily obscured rapid black-hole phase, which is ultimately preceded by an unobscured quasar phase (Alexander et al. 2005a, 2005b, Hopkins et al. 2005).

5.2. Accretion history of the Universe

Our measure of the HXLF cosmological evolution directly constrains the history of the formation of supermassive black holes (SMBH) in the galactic centers not only for luminous un-obscured AGN, that can be traced also at longer wavelengths (optical, soft X-rays), but also for the less luminous or obscured AGN. Starting from our best fit HXLF it is possible to derive the *intrinsic* (i.e. before absorption) luminosity density in the 2–10 keV band in the Universe as a function of redshift:

$$\int L_X \Phi(L_X, z) d\text{Log} L_X. \quad (15)$$

This quantity can be converted into the energy density production rate per comoving volume by means of a bolometric correction factor K ($L_{\text{bol}} = K L_X$). The mass inflow rate onto a SMBH, \dot{M}_\bullet , is related to the bolometric luminosity of the AGN, L_{bol} , by $\dot{M}_\bullet = L_{\text{bol}}(1 - \epsilon)/\epsilon c^2$, where ϵ is the radiative efficiency of the accretion flow (typically taken to be about 0.1; see e.g. Yu & Tremaine

2002, Marconi et al. 2004, Barger et al. 2005). Once a value for ϵ and K is adopted it is straightforward to derive the accretion rate density as a function of redshift:

$$\dot{\rho}_\bullet(z) = \frac{1 - \epsilon}{\epsilon c^2} \int K L_X \Phi(L_X, z) d\text{Log} L_X, \quad (16)$$

and the total accreted mass, i.e. the total density in massive black holes, if we assume that the initial mass of seeds black holes at redshift z_s is negligible with respect to the total mass:

$$\rho_{\text{BH}}(z) = \int_z^{z_s} \dot{\rho}_\bullet(z) \frac{dt}{dz} dz. \quad (17)$$

In the top panel of Figure 20 we show our direct estimate of the *intrinsic* luminosity density in the 2–10 keV band as a function of redshift from our best fit HXLF. Assuming $\epsilon = 0.1$ and the luminosity dependent bolometric correction extensively discussed by Marconi et al. (2004; their eq. 21), the total density of massive black holes as a function of redshift reported in Figure 20 is obtained by integration of the HXLF starting from $z_s = 4.5$, for $L_X > 10^{41}$ erg s $^{-1}$ and $N_H < 10^{26}$ cm $^{-2}$ (as explained in §3.4). The final accreted mass correspond to a black hole mass density in the local Universe of $\rho_{\text{BH}} = 3.2 h_{70}^2 \times 10^5 \text{ M}_\odot \text{ Mpc}^{-3}$. A somewhat higher value $\rho_{\text{BH}} = 4.0 h_{70}^2 \times 10^5 \text{ M}_\odot \text{ Mpc}^{-3}$ is obtained for a single valued bolometric correction factor $K = 40$ (Elvis et al. 1994). These results are consistent, within the errors, with the SMBH density estimate of $\rho_{\text{BH}} = 4.6^{+1.9}_{-1.4} h_{70}^2 \times 10^5$ derived from dynamical studies of local galaxies bulges (see e.g. Marconi et al. 2004 and Ferrarese 2002). As shown in Figure 20, the vast majority of the accretion rate density and black hole mass is produced by the low luminosity AGN ($L_X < 10^{44-45}$ erg s $^{-1}$) down to redshift $z \sim 1$. As already shown by the LDDE model of the HXLF, high luminosity AGN are already formed at redshift ~ 2 while low luminosity AGN keep forming down to $z \sim 1$. This result is in qualitative agreement with semi-analytical models for galaxy formation and star formation rates, such as those of Balland et al. (2003), Menci et al. (2004), Granato et al. (2004), or with the hydrodynamical simulations such as those of Di Matteo et al. (2005), Springel et al. (2005), and Hopkins et al. (2005).

6. CONCLUSIONS

We have devised a method to compute the AGN HXLF which allow us to correct for both the spectroscopic incompleteness of the faint samples, and for the selection effects due to the X-ray K-correction. Thanks to this method we have been able to collect a sample of about 500 AGN up to $z = 4$. The most important results can be summarized as follows:

- There is evidence that the fraction of absorbed ($N_H > 10^{22} \text{ cm}^{-2}$) AGN decreases with the X-ray luminosity, and increases with the redshift.
- the AGN HXLF up to $z=4$ is best represented by a LDDE model where the low luminosity ($L_X \sim 10^{43}$ erg s $^{-1}$) AGN peak at $z \sim 0.7$ while high luminosity AGN ($L_X > 10^{45}$ erg s $^{-1}$) peak at $z \sim 2$.

- We can rule out a PLE model on the basis of several arguments which take into account the discrepancies with the optical and hard X-ray LF of AGN1, and the over-predictions of the soft X-ray counts and XRB intensity.
- We estimate a density of supermassive black holes in the local Universe of $\rho_{BH} = 3.2 h_{70}^2 \times 10^5 \text{ M}_{\odot} \text{ Mpc}^{-3}$, which is consistent with the recent estimates of local galaxies black hole mass function.

The authors are grateful to the referee for helpful comments and constructive criticism improving the manuscript. We acknowledge A. Marconi for useful discussions, G. Hasinger, and A. Moretti for having provided data in machine readable format, and P. Tozzi for having provided the N_H measurements of the sources in the CDF-S sample before publication. This research has been partially supported by ASI, INAF-PRIN 270/2003 and MIUR Cofin-03-02-23 grants.

REFERENCES

- Akiyama, M., Ueda, Y., Ohta, K., Takahashi, T., Yamada, T. et al. 2003, *ApJS*, 148, 275
- Alexander, D.M., et al. 2003, *AJ*, 126, 539
- Alexander, D.M., et al. 2005a, *Nature*, 434, 738
- Alexander, D.M., Bauer, F.E., Chapman, S.C., Smail, I., Blain, A.W., Brandt, W.N., Ivison, R.J. 2005b, *ApJ*, in press (astro-ph/0506608)
- Anders, E., Grevesse, N., 1989, *Geochim. Cosmochim. Acta*, 53, 197
- Antonucci, R. 1993, *ARA&A*, 31, 473
- Baldi, A., Molendi, S., Comastri, A., Fiore, F., Matt, G., Vignali, C. 2002, *ApJ*, 564, 190
- Balland, C., Devriendt, J.E.G., Silk, J. 2003, *MNRAS*, 343, 107
- Barger, A.J., et al. 2003, *AJ*, 126, 632
- Barger, A.J., Cowie, L.L., Mushotzky, R.F., Yang, Y., Wang, W.-H., Steffen, A.T., Capak, P. 2005, *AJ*, 129, 578
- Bauer, F.E., Alexander, D.M., Brandt, W.N., Schneider, D.P., Treister, E., Hornschemeier, A.E., & Garmire, G.P., 2004, *AJ*, 128, 2048
- Bianchi, S., Guainazzi, M., Matt, G., Chiaberge, M., Iwasawa, K., Fiore, F., Maiolino, R., 2005, *A&A*, in press (astro-ph/0507323)
- Boyle, B.J., Georgantopoulos, I., Blair, A.J., Stewart, G.C., Griffiths, R.E., Shanks, T., Gunn, K.F., Almaini, O. 1998, *MNRAS*, 296, 1
- Boyle, B.J., Shanks, T., Croom, S.M., Smith, R.J., Miller, L., Loaring, N., Heymans, C. 2000, *MNRAS*, 317, 1014
- Brandt, W.N., Hasinger, G. 2005, *ARA&A*, 43, in press (astro-ph/0501058)
- Brusa, M. et al. 2003, *A&A*, 409, 65
- Caccianiga, A., et al. 2004, *A&A*, 416, 901
- Cocchia et al. 2005, *A&A*, submitted
- Comastri, A., Setti, G., Zamorani, G., Hasinger, G. 1995, *A&A*, 296, 1
- Comastri, A., Fiore, F., Vignali, C., Matt, G., Perola, G.C., La Franca, F. 2001, *MNRAS*, 327, 781
- Cowie, L.L., Barger, A.J., Bautz, M.W., Brandt, W.N., Garmire, G.P. 2003, *ApJ*, 584, L57
- Croom, S.M., Smith, R.J., Boyle, B.J., Shanks, T., Miller, L., Outram, P.J., Loaring, N.S. 2004, *MNRAS*, 349, 1397
- De Luca, A & Molendi, S. 2004, *A&A*, 419, 837
- Di Matteo, T., Springel, V., & Hernquist, L. 2005, *Nature*, 433, 604
- Elvis, M., et al. 1994, *ApJS*, 95, 1
- Fasano, G. & Franceschini, A. 1987, *MNRAS*, 225, 155
- Ferrarese, L., 2002, *ApJ*, 578, 90
- Fiore, F., et al. 2000, *New A*, 5, 143
- Fiore, F., et al. 2003, *A&A*, 409, 79
- Gehrels, N. 1986, *ApJ*, 303, 336
- Georgantopoulos, I., Stewart, G.C., Shanks, T., Boyle, B.J., Griffiths, R.E. 1996, *MNRAS*, 280, 276
- Giacconi, R., et al. 2002, *ApJS*, 139, 369
- Gilli, R., Risaliti, G., Salvati, M. 1999, *A&A*, 347, 424
- Gilli, R., Salvati, M., Hasinger, G. 2001, *A&A*, 366, 407
- Granato, G., De Zotti, G., Silva, L., Bressan, A., Danese, L. 2004, *ApJ*, 600, 580
- Grossan, B.A., 1992, Ph. D. Thesis, MIT, Cambridge
- Halpern, J.P., Eracleous, M., Forster, K. 1998, *ApJ*, 501, 103
- Hasinger, G., 2003, in *AIP Conf. Proc.* 666, *The Emergence of Cosmic Structure*, ed. S.S. Holt & C. Reynolds (New York: AIP), 227
- Hasinger, G., Miyaji, T., Schmidt, M. 2005, *A&A*, in press (astro-ph/0506118)
- Hopkins, P.F., Hernquist, L., Martini, P., Cox, T.J., Robertson, B., Di Matteo, T., & Springel, V. 2005, *ApJ*, in press (astro-ph/0503055)
- Kinzer R.L., Jung G.V., Gruber D.E., Matteson J.L., Peterson L.E. 1997, *ApJ*, 475, 361
- La Franca, F., Franceschini, A., Cristiani, S., & Vio, R. 1995, *A&A*, 299, 19
- La Franca, F., Cristiani, S. 1997, *AJ*, 113, 1517
- La Franca, F., et al. 2002, *ApJ*, 570, 100
- Lampton, M., Margon, B., Bowyer, S. 1976, *ApJ*, 207, 894
- Mainieri, V., Bergeron, J., Hasinger, G., Lehmann, I., Rosati, P., Schmidt, M., Szokoly, G., & Della Ceca, R. 2002, *A&A*, 393, 425
- Maiolino, R. & Rieke, G.H., 1995, *ApJ*, 454, 95
- Maccacaro, T., Della Ceca, R., Gioia, I.M., Morris, S.L., Stocke, J.T., Wolter, A. 1991, *ApJ*, 374, 117
- Marconi, A., Risaliti, G., Gilli, R., Hunt, L.K., Maiolino, R., Salvati, M. 2004, *MNRAS*, 351, 169
- Marshall F.E., Boldt E.A., Holt S.S., Miller R.B., Mushotzky R.F., Rose L.A., Rothschild R.E., Serlemitsos P.J. 1980, *ApJ*, 235, 4
- Menci, N., Fiore, F., Perola, G. C., Cavaliere, A. 2004, *ApJ*, 606, 58
- Mignoli, M. et al. 2004, *A&A*, 418, 827
- Miyaji, T., Hasinger, G., Schmidt, M. 2000, *A&A*, 353, 25
- Moretti, A., Campana, S., Lazzati, D., Tagliaferri, G. 2003, *A&A*, 403, 297
- Morrison, R., McCammon, D.A., 1983, *ApJ*, 270, 119
- Norman, C. et al. 2002, *ApJ*, 571, 718
- Padovani, P., Allen, M.G., Rosati, P., Walton, N.A. 2004, *A&A*, 424, 545
- Page, M.J., et al. 2003, *Astronomische Nachrichten*, 324, 101
- Panessa, F., Bassani, L. 2002, *A&A*, 394, 435
- Perola, G.C., et al. 2004, *A&A*, 421, 491
- Piccinotti, G., Mushotzky, R.F., Boldt, E.A., Holt, S.S., Marshall, F.E., Serlemitsos, P.J., Shafer, R.A. 1982, *ApJ*, 253, 485
- Pompilio, F., La Franca, F., Matt, G., 2000, *A&A*, 353, 440
- Ranalli, P., Comastri, A., Setti, G. 2003, *A&A*, 399, 39
- Revnivtsev, M., Gilfanov, M., Sunyaev, R., Jahoda, K., Markwardt, C. 2003, *A&A*, 411, 329
- Revnivtsev, M., Gilfanov M., Jahoda, K., Sunyaev, R., 2004, *A&A*, submitted (astro-ph/0412304)
- Risaliti, G., Maiolino, R., Salvati, M. 1999, *ApJ*, 522, 157
- Setti, G., Woltjer, L., 1989, *A&A*, 224, L21
- Silverman, J.S., et al. 2005, *ApJ*, 618, 123
- Steffen, A.T., Barger, A.J., Cowie, L.L., Mushotzky, R.F., Yang, Y. 2003, *ApJ*, 506, L23
- Szokoly, G. P., et al. 2004, *ApJS*, 155, 271
- Tozzi, P. et al. 2005, *A&A*, submitted
- Treister, E. et al. 2004, *ApJ*, 616, 123
- Treister, E. & Urry, C.M. 2005, *ApJ*, in press (astro-ph/0505300)
- Ueda, Y., Akiyama, M., Ohta, K., Miyaji, T. 2003, *ApJ*, 598, 886
- Vignati, P. et al. 1999, *A&A*, 349, L57
- Yu, Q., Tremaine, S. 2002, *MNRAS*, 335, 965
- Zheng, W., et al. 2004, *ApJS*, 155, 73
- Zombeck, M.V. 1990, *Handbook of Space Astronomy and Astrophysics* (Cambridge University Press)